MATHEMATICAL AND PHYSICAL MODELLING OF

DIRECTIONAL SOLIDIFICATION OF AEROSPACE ALLOYS

by

Christy S. Choi

B.S. Materials Science and Engineering

Massachusetts Institute of Technology (1993)

Submitted to the Department of Materials Science and Engineering
in Partial Fulfillment of the Requirements for the Degree of

MASTER OF SCIENCE IN MATERIALS ENGINEERING

at the

MASSACHUSETTS INSTITUTE OF TECHNOLOGY

June, 1996

Signature of Author . . . .
Department of Materials Science and Engineering
May 10, 1996

Certified by . . . .
Julian Szekely
Professor of Materials Science and Engineering
Thesis Supervisor

Accepted by . . . .
Michael F. Rubner
TDK Professor of Materials Science and Engineering
Chair, Departmental Committee on Graduate Students

A note regarding the "Certified by" entry on the cover page:

It should be known that Professor Julian Szekely supervised this thesis work until his death in December, 1995. In his absence, Professor David C. Dunand, whose signature appears in this entry, has agreed to evaluate this thesis.

MATHEMATICAL AND PHYSICAL MODELLING OF

DIRECTIONAL SOLIDIFICATION OF AEROSPACE ALLOYS

by

Christy S. Choi

Submitted to the Department of Materials Science and Engineering
on May 10, 1996 in partial fulfillment of the requirements for the
Degree of Master of Science in Materials Engineering

ABSTRACT

Defect formation in aerospace components is studied, particularly in regions of directionally solidified casting with stepwise increase in cross-section, which is a typical geometric configuration for such components as turbine blades. Given the fact that the geometry of a casting is directly related to probability of defect formation, special attention was paid to grain defects in regions of cross-sectional change (platform regions). Mathematical and physical modelling were employed to describe directional solidification and to obtain overall understanding of different or key aspects involved in the directional solidification process. Aluminum-4.5wt%Copper alloy was used for physical modelling; mathematical models were made both of the Al-Cu system (for correlation to the physical model) and of In718, a nickel-based superalloy (for correlation to actual defective parts examined). Although characteristically different, analysis of the solidification pattern of the two materials showed some commonalities, such as primary dendritic growth orientation and location of defect formation. The combination approach to modelling, employing both mathematical and physical methods, led to a good understanding of the process, and increased the ability to design new configurations whose solidification patterns promote single crystals with minimum defects.

Thesis Supervisor: Julian Szekely
Title: Professor of Materials Science and Engineering

In Loving Memory of

Professor Szekely

ACKNOWLEDGMENTS

TABLE OF CONTENTS

NOMENCLATURE

A	=	surface area
A	=	growth kinetics constant
α	=	thermal diffusivity
β	=	thermal expansion coefficient
C_o	=	initial composition
C_e	=	eutectic composition
C_L	=	composition at liquidus
C_p	=	specific heat
C_S	=	composition at solidus
C_v	=	volumetric heat capacity
D	=	diffusivity
d	=	lateral extension of cross-section
Ei	=	exponential integral function
ε	=	emissivity
G	=	thermal gradient
G_c	=	solutal gradient
Gr	=	Grashof number
Γ	=	Gibbs-Thomson coefficient
g	=	gravity
γ	=	surface tension
Iv	=	Ivantsov function
k	=	thermal conductivity
k	=	partition coefficient
L	=	characteristic dimension

λ_1	=	primary dendrite trunk spacing
λ_2	=	secondary dendrite arm spacing
M_1	=	constant for λ_1 calculation
M_2	=	constant for λ_2 calculation
m	=	slope of liquidus
μ	=	viscosity
Nu	=	Nusselt number
ν	=	kinematic viscosity
Pe	=	Peclet number
Pr	=	Prandtl number
R	=	radius of dendrite tip
Ra	=	Rayleigh number
Re	=	Reynolds number
ρ	=	density
q	=	heat flux
ΔS_f	=	volumetric entropy
σ	=	Stefan-Boltzmann constant
T	=	temperature
T_o	=	initial temperature
T_w	=	wall temperature of furnace
ΔT	=	lateral temperature difference
ΔT	=	undercooling
ΔT_o	=	solidification interval of alloy
ΔT_1	=	primary undercooling
ΔT_2	=	secondary undercooling

t_f	=	local solidification time of alloy
τ	=	decay time (turbulence)
u	=	relative velocity of fluid
V	=	volume
v	=	global solidification speed

LIST OF FIGURES

LIST OF TABLES

1. INTRODUCTION

1.1 Modelling of Casting of Aerospace Alloys

Technology plays many important roles in materials processing today, especially in manufacture of aerospace parts, since they require precision to produce, which can be improved with technology-aided processing methods. Although production of aerospace components have benefited greatly from recent technological advances, there still remain a number of important ways in which technology can help to improve further the efficiency and the quality of production. A very effective and efficient way is to predict intelligently the quality of cast parts before making any substantial changes in actual manufacture lines by simulating, or modelling, a critical step of a manufacturing process.

Two kinds of modelling are generally used: physical (sometimes called experimental) and mathematical (computational). Physical modelling usually employs a processing system similar to an actual process, the main differences being the scale of the system and/or the materials used (for cost reasons or for better observability). Mathematical modelling is generally done with the help of a computer, which can perform complicated calculations very fast, and us es as the basis of simulation equations relevant to the mechanism or physical phenomena taking place in the system being studied.

These two methods, when used together, can provide a great amount of useful information on the system being studied. Displaying the procedure and effectiveness of a

12

joint modellilng method, by using the case of directional solidification of aerospace alloys, is one of the main purposes of this thesis. In addition, this paper suggests a time-efficient yet accurate way of modelling by this combination approach so it can be a practical addition to academia- and industry- oriented studies involving modelling.

A number of studies have been done using modelling to examine casting of aerospace alloys, some of which have been by General Electirc-Wright Patterson Laboratory, DARPA, and Howmet. This thesis is based on a research project carried out for a consortium on casting of aerospace alloys, organized and sponsored by the National Institute of Standards and Technology. A task for the consortium was to devise a way to combine both macroscale and microscale modelling of solidification; that is, to establish a method which deals with the solidification process both on a macro-scale with such issues as bulk fluid flow and heat transfer, and on a micro-scale, involving solutal diffusion, dendrite formation, and heat conduction. This comprehensive approach is more efficient and effective for gaining overall understanding of the casting process than using only one type of analysis.

This thesis investigates the making of investment cast alloys by directional solidification. In order to have good high temperature creep properties, many aerospace alloys are directionally solidified. Single crystal structure in directional solidification is achieved either by planting a "seed" in the bottom part of the mold or by using a grain selector, a spiral-shaped cavity in the bottom of a casting, to be cut away afterwards, that selects geometrically one orientation of grain over others.

In investment casting, molten metal is poured inside a mold, usually with complex geometrical shapes. Then a temperature gradient is imposed along the length of the casting by a surrounding furnace, parallel to the desired direction of grain growth. Then the

casting is moved along the direction of the desired grain growth (for turbine blades, this direction of casting withdrawal is called "stacking axis of turbine blade"), i.e., along the direction of the temperature gradient. Solidification then takes place via transport mechanisms such as heat and mass transfer. Application of appropriate processing conditions such as the withdrawal rate of the casting and temperature gradient will help minimize defect formation.

Another goal of this thesis is to examine directional solidification of aerospace alloys, specifically, an aluminum-based alloy and a nickel-based superalloy, studying defect formations in regions of sudden cross sectional changes. This stepwise cross-sectional change is a typical geometric configuration for a number of aerospace components such as turbine blades. A way to study formation of defects is to concentrate on transport phenomena involved in solidification. This is done here by combining the two modelling methods described above, with the addition of an analytical approach based on relevant dimensionless numbers describing transport phenomena.

Many defects can form during a manufacture process of aerospace components. Defect formation can slow down the production rate and at the same time increase the cost involved, since as a rule defect parts are discarded and not re-melted for recasting. In order to determine ways to minimize defects, a good understanding of detect formation mechanisms is necessary. One of the main objectives of this thesis is to gain such understanding on some of the defects, namely, those associated with a sudden change in cross-section, specifically in the platform region which is typical on the geome ry of a turbine blade. This is achieved by combining physical and mathematical modelling.

Figure 1-1 displays a schematic sketch of a turbine blade with common grain defects [1]. For example, bi-grains form when more than one grain emerges from the

14

100 PRIMARY CRYSTALLOGRAPHIC
DIRECTION

STACKING AXIS OF
TURBINE BLADE

PRIMARY MISORIENTATION
(Usually up to 10-15° permitted)

SECONDARY GRAIN
High angle grain
which nucleated &
grew from the melt
in competition with
the primary grain.

ZEBRA GRAINS
An array of multiple low
angle boundaries
exhibiting high reflectivity
between adjacent areas.
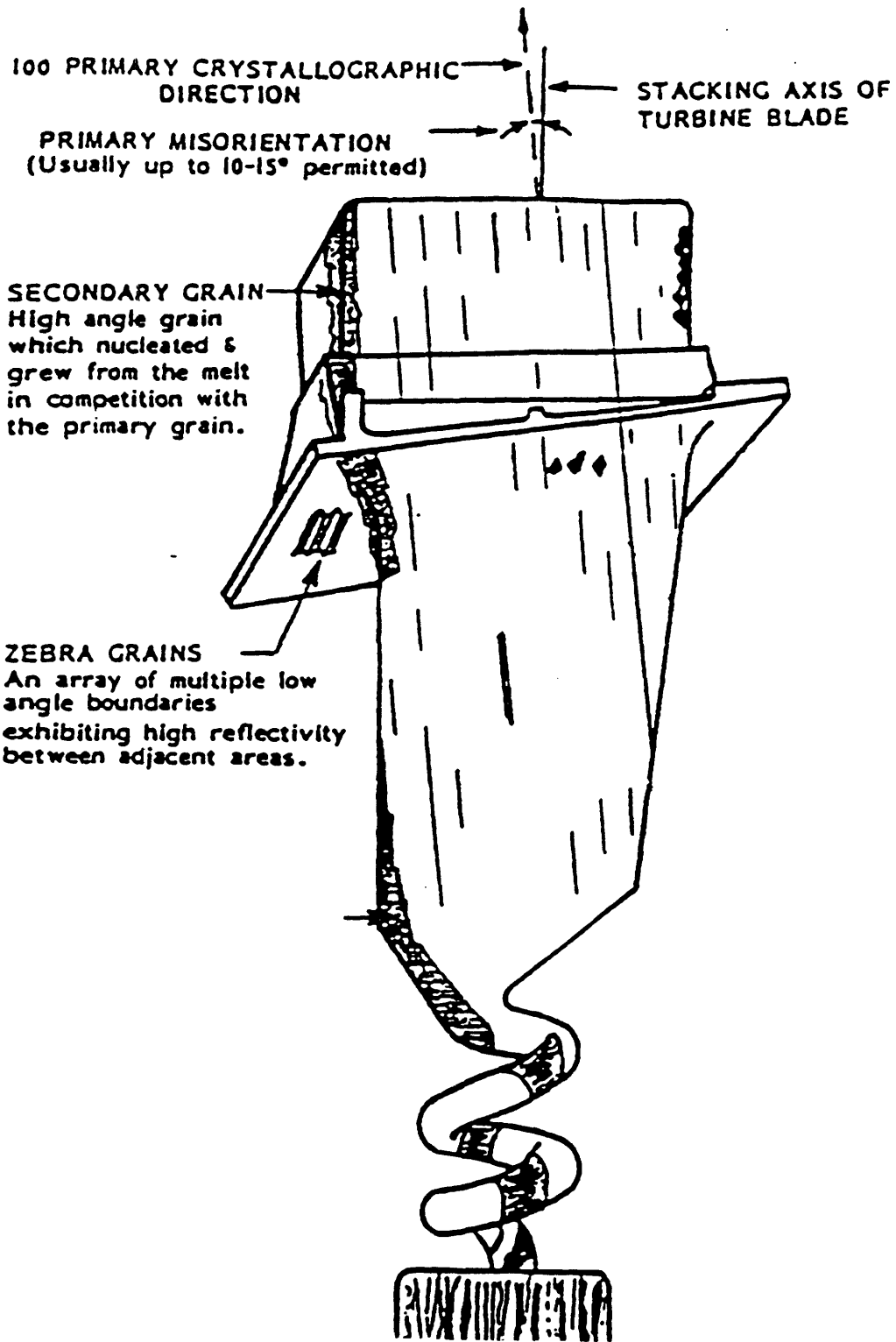
Fig.1-1. Grain defects in single crystal turbine blades.

grain selector, the spiral-shaped part at the bottom of the mold. Secondary grains form

mainly as a result of a new nucleation from the melt, separate from the primary grain.

Other defects include: freckles (on the upper right part of the figure); recrystallized grain

(shown as a cluster of little dots beneath the platform region); and sliver (in the center).

The point of interest in the structure for this thesis is the platform region, usually

prone to defects due to stray grains and zebra grains. A stray grain usually forms as a

result of dendrite remelting due to local concentration gradient and undercooling. Zebra

grains, usually originating from stray grains [2], are highly reflective, and can be detected

visually upon close visual examination of the platform region.

In this thesis, directionally solidified turbine blade parts prone to defect formation

due to a sudden increase in cross-section were studied in the following manner. First, the

casting process was modelled physically. Next, the solidification phenomena were

examined using relevant equations of heat and mass transfer describing the system on a

macroscale.

Then computational modelling of the solidification process was performed using a

computer simulation software called ProCAST™, as suggested by the consortium, with a

focus on macoscale solidification phenomena. First, the solidification process was

simulated with the values obtained from the physical modelling in order to observe

numerically and understand the solidification phenomena in the physical model, then by

varying some of the processing conditions used in the experiments in order to determine a

set of optimum processing conditions which would help minimize defect formation, thus

improving the overall quality and efficiency of production.
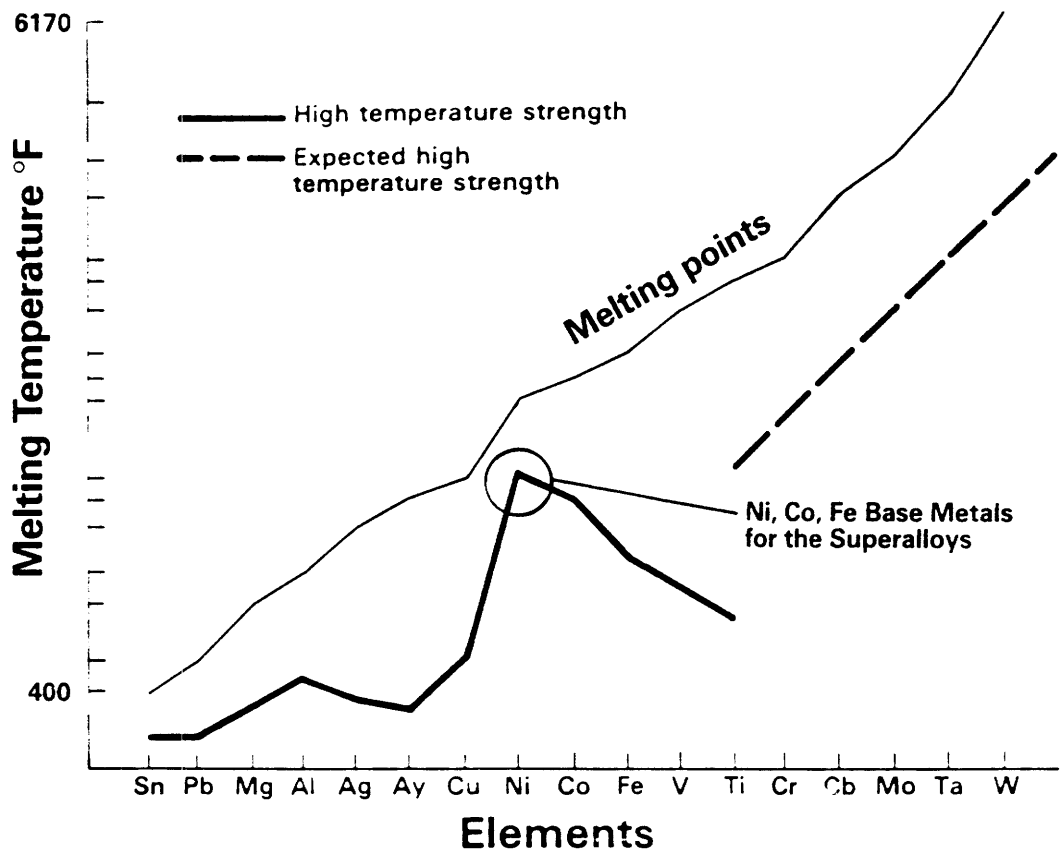
Fig.1-2. High temperature strength of various elements.

1.2 Materials for Analysis

Figure 1-2 shows high temperature strength of various elements with melting temperature[3]. The higher the melting temperature of a material, the costlier and more difficult it is to handle it. Therefore, materials with good high temperature strength as well as relatively low melting temperature are desirable for study as well as manufacture. Aluminum, while having a relatively low melting point, exhibits a relatively high strength compared to elements with similar melting points. Similarly, nickel has very good high temperature strength for its melting point.

Two materials, an aluminum-copper alloy and a nickel-based superalloy, were used for modelling. The Al-Cu alloy's copper content was 4.5 wt% and was manufactured expressly for this research at the National Institute of Science and Technology in Gaithersburg, Maryland. It was used in the physical modelling done at NIST and served as a representative alloy for dendritic arm spacing and undercooling calculations in the analytical section, as well as providing the starting point for computational modelling. A potentially big problem with using an aluminum alloy was its tendency for easy oxidation, and an experimental method was necessary which would minimize its coming into contact with oxygen while in a molten state (further discussed in Chapter 2).

For a nickel-based alloy, Inconel 718 was chosen, largely because it is one of the materials that are actually used for turbine blade manufacture. As shown in Table 1-1, IN718 is about 53% Ni (base metal), with Cr and Fe as major components.

Table 1.1. Composition of Inconel 718 [4].

| Ni | 52.5% |

18

Cr	19.0%
Fe	18.5%
Nb	5.1%
Mo	3.0%
Ti	0.9%
Al	0.5%
Cu	0.15% max
C	0.08%

IN718 was used as the high-melting-point material in the computational analysis, as well as in sensitivity analysis using dimensionless numbers and radiation-based solidification time calculation.

The overall modelling procedure using these two materials was as follows. First, physical modelling with the Al-Cu system, the cast samples were examined for structure and defects. Also, defect parts made of In718 from an actual manufacture line were examined for defect distribution. Then, order of magnitude analysis (with dimensionless numbers) was done to describe the experiments of the physical modelling, as well as to predict the behavior of In718 by determining the nature of its fluid flow under various processing conditions.

Next, computational simulation was performed using a geometry based on that of the physical modelling. For Al-Cu, the values obtained from the experimental setup and the numerical analysis were used first to test and verify the accuracy of the simulation program, followed by changes in some of the processing conditions in order to observe effects of different processing parameters such as temperature gradients and to determine an optimum set of processing conditions. Solidification of In718 was simulated, some of

whose initial values were modified from those of the Al-Cu runs. Then changes were made in some of the parameters. Finally, necessary changes to the solidification procedure was determined, such as temperature, solidification speed, and the geometry.

2. PHYSICAL MODELLING

2.1 Introduction

The experimental component of the research was mostly carried out at the National Institute of Standards and Technology in Gaithersburg, MD, with the direct supervision of Dr. R. J. Schaefer. The main component of the experimental work was physical modelling of directional solidification in casting of aerospace alloys, with Al-4.5%Cu as the metal and alumina as the mold material. Additional work includes: optical microscopic analysis of the cast parts; and examination of defects found in actual parts from actual manufacture lines.

The physical model served as a starting point of the research, yielding values for the casting conditions such as the geometry, initial temperatures, temperature gradients, cast and mold materials and their properties, and solidification speed, which were later used in numerical analyses, including the computer simulations presented in this thesis. Another important purpose of the physical model was to generate sample castings with cross-sectional changes to be examined for dendritic growth pattern and location of defects on the platform region with a cross-sectional increase, as will be described in more detail subsequently in this chapter). These results were later compared to the solidification patterns obtained by computational simulations. Also to be noted were any similarities between the experimentally cast parts and the manufactured parts in regards to defect formations and the relative orientations of primary and secondary grains.

It should be stressed that no attempt was made to establish an accurate similarity (dynamic, thermal or geometric) between the system selected in this experimental part (i.e., Al-Cu) and the actual system (i.e., investment casting of Ni-based turbine blades). This is because these experiments were established as a preliminary effort to gain some overall understanding of the defect problem by using a system with a low melting point.

Additional analysis was performed on the manufactured parts that were mostly turbine blade parts with platform regions defects. Areas on the platform section of the parts, where most visible defects such as stray grains and zebra grains were located, were examined using X-ray diffraction as well as SEM. The main purpose of this investigation, in addition to providing the basis for comparison for the experimental parts, was to establish any patterns in the location of a defect and its orientation relative to the main dendritic structure.

2.2 Furnace Setup and Specifications

Physical models were built to describe the directional solidification process, which were performed using a vertically moving furnace (Figure 2-1). The furnace had a cylindrical cavity of approximately 5/8'' in diameter at its center. The temperature of the furnace was monitored with seven thermocouples, one of which, placed in between the inner furnace wall and the outer mold wall, was used to control the set temperature automatically (Figure 2-2). The vertical position of the furnace, which moved with respect to the stationary mold, was also automatically monitored. The speed of the movement of the furnace itself could be varied, upward or downward, from 0.05 to 0.4 cm/min. Water ran through the bottom of the furnace as a coolant. The temperature fluctuation was
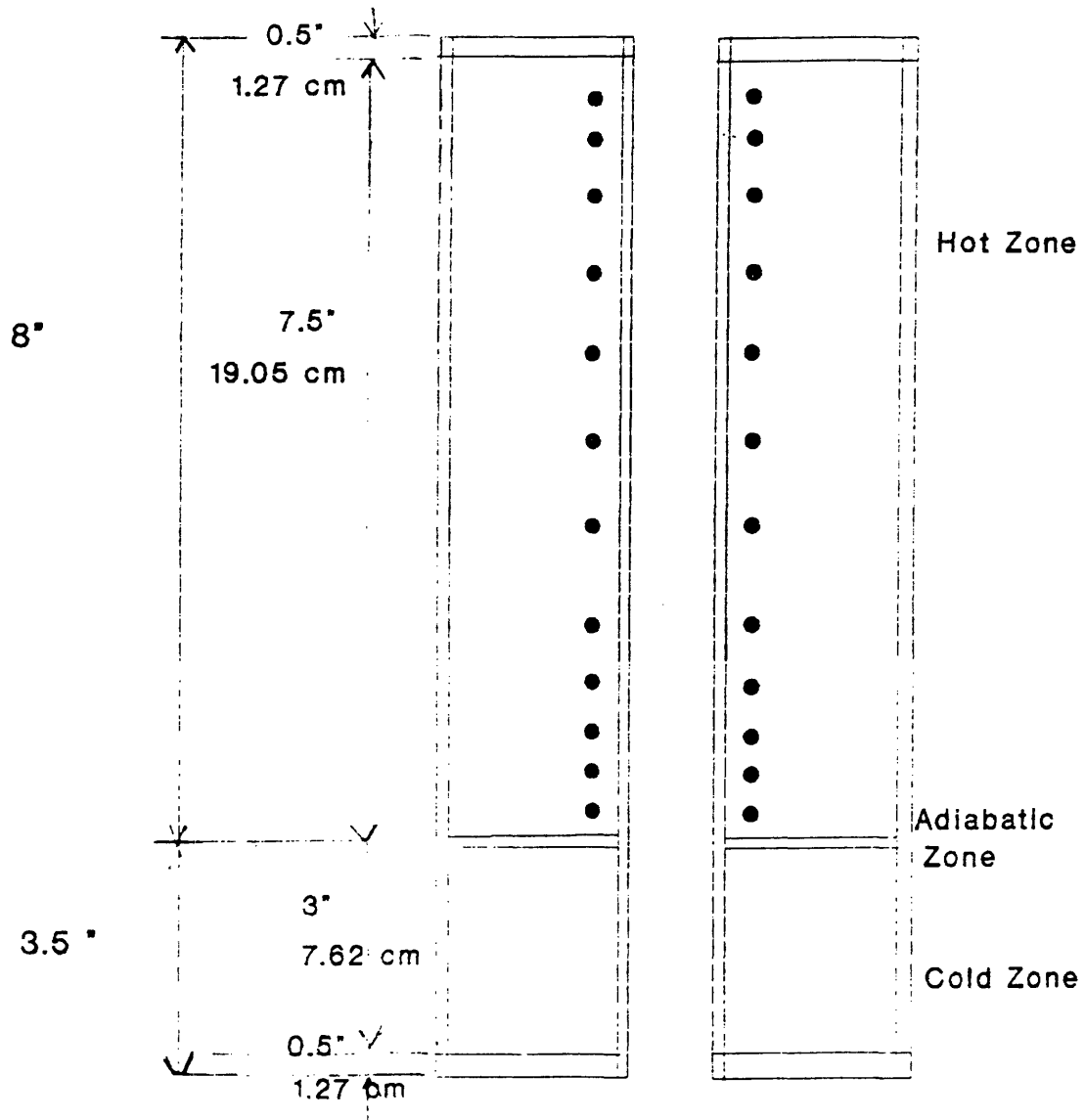
Fig.2-1. Schematic of directional solidification furnace.
Dots indicate heating element locations.
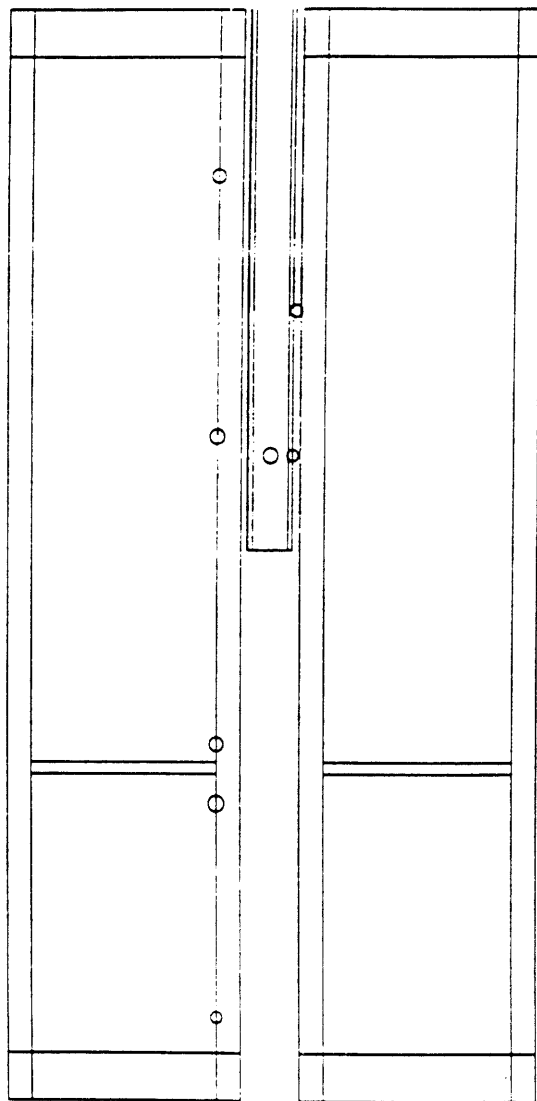
Fig.2-2. Locations of thermocouples in furnace, represented by circles.

usually within ±1 K, except for some irregular fluctuations of a bigger magnitude which seemed to be the result of any changes in the flow rate and/or the temperature of the cooling water. The vertical length of the hot zone of the furnace was approximately 20 cm, while the chill zone was 9 cm long.

The molds, made of alumina tubes, included an additional fixture at the bottom end, made of machinable ceramic, whose purpose was to provide horizontal cross sectional variation in the mold. The two components of the mold were glued together, then was fired to seal where the glue had been applied. Figure 2-3 illustrates the bottom part of the vertical cross section of the mold with solidified metal inside. The outermost vertical lines indicate the inner wall of the furnace. The white part corresponds to the mold. As seen in the figure, the thickness of the mold wall was a little less than 1/16" on the side and thicker on the bottom and around the lower part of the casting. The lengths of the tubes were usually between two and three feet. The top of the tube was attached to a vacuum pump that would keep the space above the molten metal at a near vacuum state ($\sim 10^{-6}$ atm.) except when argon gas with pressure of one to two psi was injected to keep the molten metal down at the bottom of the mold. The height of the molten metal was usually on the order of 15 to 20 cm.
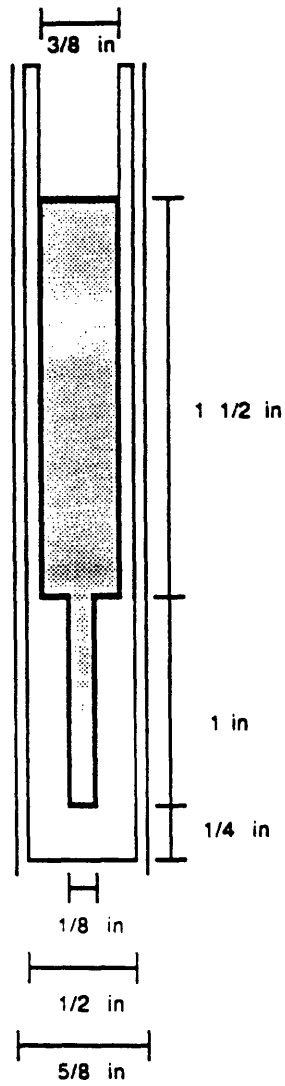
Fig.2-3. Schematic of physical modelling setup. Shaded region represents
the casting, surrounded by mold and the inner furnace wall.

2.3 Test Runs

The automated temperature control program recorded data from the seven thermocouples as well as the vertical moving position of the mold during the experiments in relation to a fixed point of the furnace. The exact temperature distribution of the furnace wall was determined by varying the control temperature, corresponding to one of the thermocouples attached at the point in the furnace communicating with the temperature controller. The rest of the thermocouples were only used as sensors for recording.

It was found, after runs with an empty mold with four different control temperatures ranging from 650°C to 800°C, that the highest temperature for a run with a given control temperature was usually 50°C-100°C higher than the control temperature, located 1-2 cm below the position of the control thermocouple (and therefore where the temperature was kept at the control value). It was also found that 700°C and 750°C as control temperatures produced very similar distribution curves, i.e., with similar gradients.

Next, observations were made for the lateral temperature difference between the inner furnace wall, the mold wall, and inside the casting, all of them with the same vertical distance. Two thermocouples were placed, one in the center of the casting and the other one on the outer wall of the mold, respectively, at the same vertical position, in order to observe the change in temperature. It was found through several heating cycles that the temperature gap between the two sides of the mold wall for a given height varied depending on the temperature. That is, at lower temperatures, the outer mold wall was at a slightly higher temperature than the center of the casting, and the reverse was true for higher temperatures. The temperature range in which this change occurred was a little above the liquidus of the Al-Cu alloy.

higher temperature than the center of the casting, and the reverse was true for higher temperatures. The temperature range in which this change occurred was a little above the liquidus of the Al-Cu alloy.

Next, to observe the effect of the molten metal in the mold on the temperature distribution, and to verify casting conditions such as the gas pressure and solidification speed, test runs were performed using soldering wire made of antimony-tin alloy. For this low-melting alloy, both alumina and glass molds were used, the latter enabling visual observation of the cast piece without having to cut open the mold. After the processing conditions were verified, the aluminum-copper alloy was introduced for the experiments.

2.4 Casting and Optical Examination of Al-4.5%Cu

The alloy used for the experiments was made on the premise according to the specifications of 95.5wt% aluminum and 4.5wt% copper, in a cylindrical shape with the diameter slightly smaller than the inside diameter of the mold. The general procedure of experiments was as follows. First, a rod of Al-Cu alloy was cleaned, then cut to a desired length. Then the rod was placed in the mold, which in turn was placed through the furnace and attached to the gas pump at the top. The furnace, which was kept at approximately 200°C, was then heated up to the set point, for which 750°C proved to be the most effective among the temperatures tested. The linear temperature gradient in the furnace for the melting range of the Al-4.5%Cu alloy was 65 to 70 K/cm in the vertical direction of the furnace (Figure 2-4).

After being held stationary once the set temperature was reached, the furnace was moved down at a constant rate, usually of 0.22 cm/min., heating the alloy. As the alloy
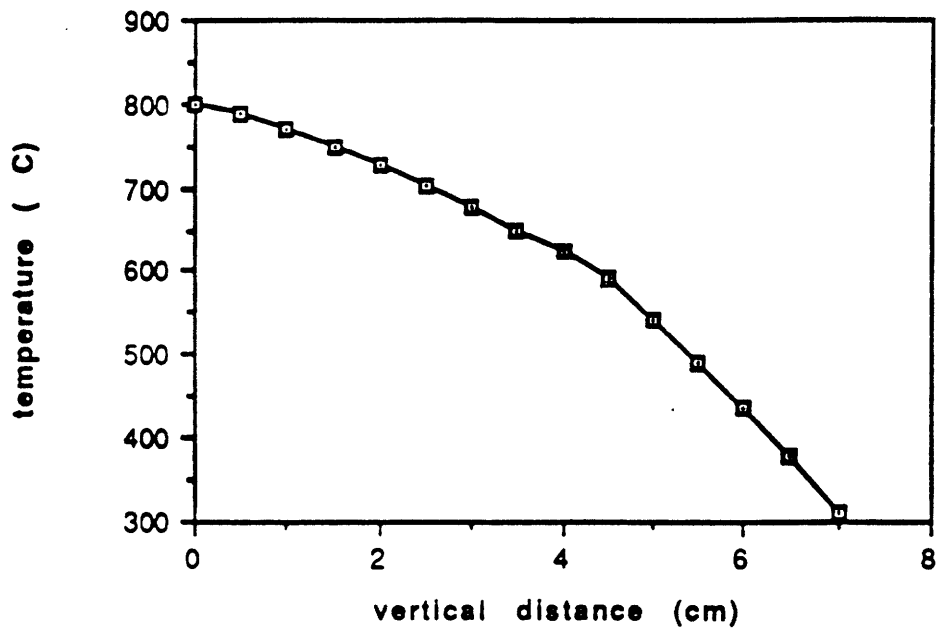
Fig.2-4. Temperature distribution in furnace. Control temperature of 750°C
yields thermal gradient of app. 65 K/m in the melting range of
Al-4.5%Cu.

was being heated, argon was blown into the mold from the top three times, pushing the molten metal to fill in the smaller cross section at the bottom of the mold which had not been occupied by the solid rod of the alloy. The reason for starting the experiment with the solid rod as opposed to pouring the alloy in its molten state into the mold was to prevent it from oxidizing, which would lead to formation of secondary grains along the boundary of the casting during the solidification stage.

When the part of the furnace that corresponded to the melting point of the alloy had reached a small distance below the bottom of the mold, the furnace was held stationary for approximately 20 minutes. Then it was raised at a constant rate which varied from one run to the next until the optimal velocity of approximately 0.15 cm/min. was found. This speed is a bit slower than the value of 0.1 mm/sec, or 0.6 cm/min., used in the study by Rappaz et al. [5] presenting the relationship between the lateral extension of a cross section and the degree of resulting undercooling of dendrites.

After the furnace was raised enough to be believed to have solidified all of the metal, the temperature of the furnace was lowered. Usually the mold was taken out from the furnace when the control temperature reached 200°C or so, then it was quenched with room temperature water. The mold was then cut parallel to its circular cross section using a diamond saw to various heights. Some cast parts were then cut vertically (either once or twice) to show the longitudinal cross section. At least two to three such sections (longitudinal and transverse) per run were mounted in epoxy and were observed with optical microscopes after being polished and sometimes etched. The etchant used was Keller's agent.

2.5 SEM and XRD analysis of defect parts

This section describes the additional laboratory work performed in conjunction with the physical modelling, namely the investigation of platform-region defects, such as stray grains and zebra grains, of turbine blade parts from actual manufacture lines. The information obtained from this analysis was used to help determine the probability of locations of such defect formation and the extent of misorientation of these defect grains relative to the orientation of the primary grain.

Microscopic measuring devices were used to examine defective parts, provided by Howmet and PCC airfoils. After locating areas of high defect density by optical examination, small parts of interest (Figure 2-5) were cut off in order to fit in SEM and XRD chambers, then mounted, polished, and etched for suitable visibility of stray grains. At NIST, electron backscattering pattern (EBSP) analysis of zebra grains, with SEM, was done by R. J. Schaefer for determination of the angles between the stack axis of the casting and the [001] direction of the primary dendrite as well as the misorientation of the zebra grains to the primary dendrite growth direction.

Next, X-ray analysis using Laue diffraction was done to try to determine the orientation of [010] and [100] axes. First, a larger triangular piece was cut from a defective component, two of whose sides were composed by outer edges of the platform, with approximately 1 cm thickness. The cut surface, which formed the base of the triangle, was approximately 10 cm long, and the height of the triangle was approximately 8 cm (Figure 2-6). After being mounted in a holder with the bottom surface of the platform facing the film, nine points were examined for misorientation angles. The outer corner of the platform being the top of the triangle, five points were marked, with a 1-cm interval, down the center of the triangle from the tip. Then, two points, also with a 1-cm interval,

GROWTH DIRECTION

SMALL GRAINS
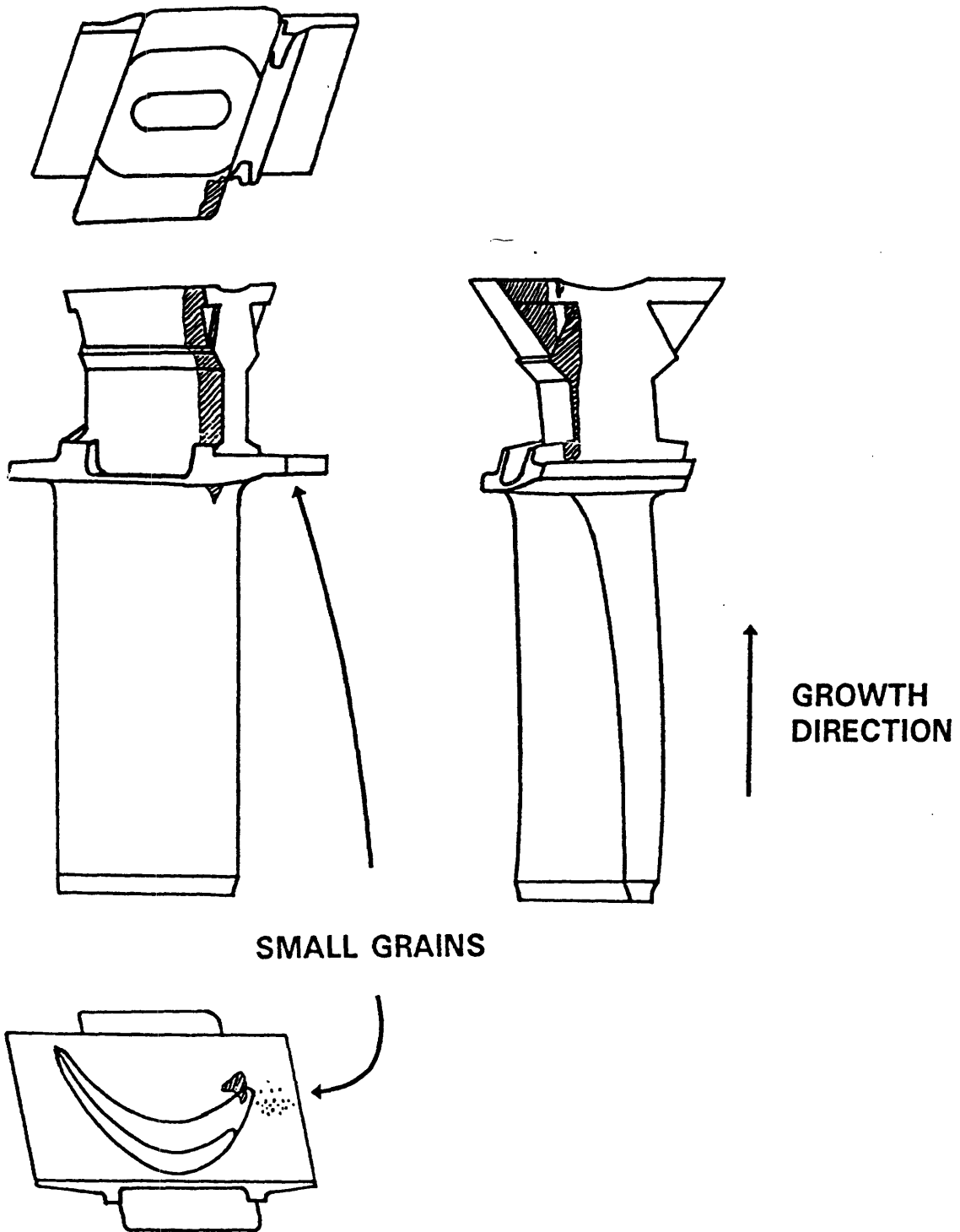
Fig.2-5. Location of grain defects on the platform of turbine blade.
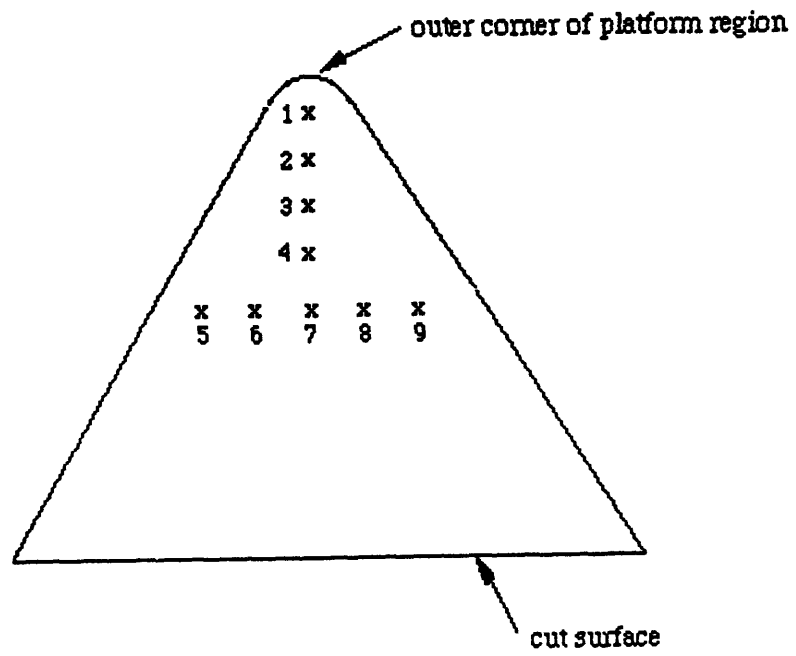
Fig.2-6. Points on the outer edge of a defectiive part examined by X-ray difraction.

were marked on either side of the lowest vertical mark, forming a reversed T. From the pictures taken of these nine points, the angles relative to the normal direction of the mounted sample, which in turn was tilted by a few degrees from the normal axis of the blade, i.e., the primary growth direction, were measured.

2.6 Results and Discussion

In the directionally solidified crystal samples of Al-Cu in the physical model, the primary dendrite arms usually propagated in the direction very close to that of the solidification (normal to the bottom of the mold). This is in good accordance with parts from actual production lines, whose misorientation angle between the direction of solidification and the direction of the primary dendritic growth is under 10°.

Figures 2-7 through 2-9 show the optical microscope pictures of various samples in various magnifications. The white lines correspond to the dendrite branches growing on (001) planes. The angle between the direction of solidification, i.e., the [001] axis of the casting, and the primary growth direction of dendrites ranged from 10° to 18°. Furthermore, in general, the dendrites started out relatively small at the bottom of the casting, grew larger and more defined in the middle, then became less distinctive near the top.

In an actual manufacture line, the beginning of the mold is usually attached to a spiral-shaped grain selector, which selects one direction of dendritic growth among many that form in the initial stage of the solidification. Such grain selection was not done in the same manner in the physical models. However, examination of the beginning parts of the
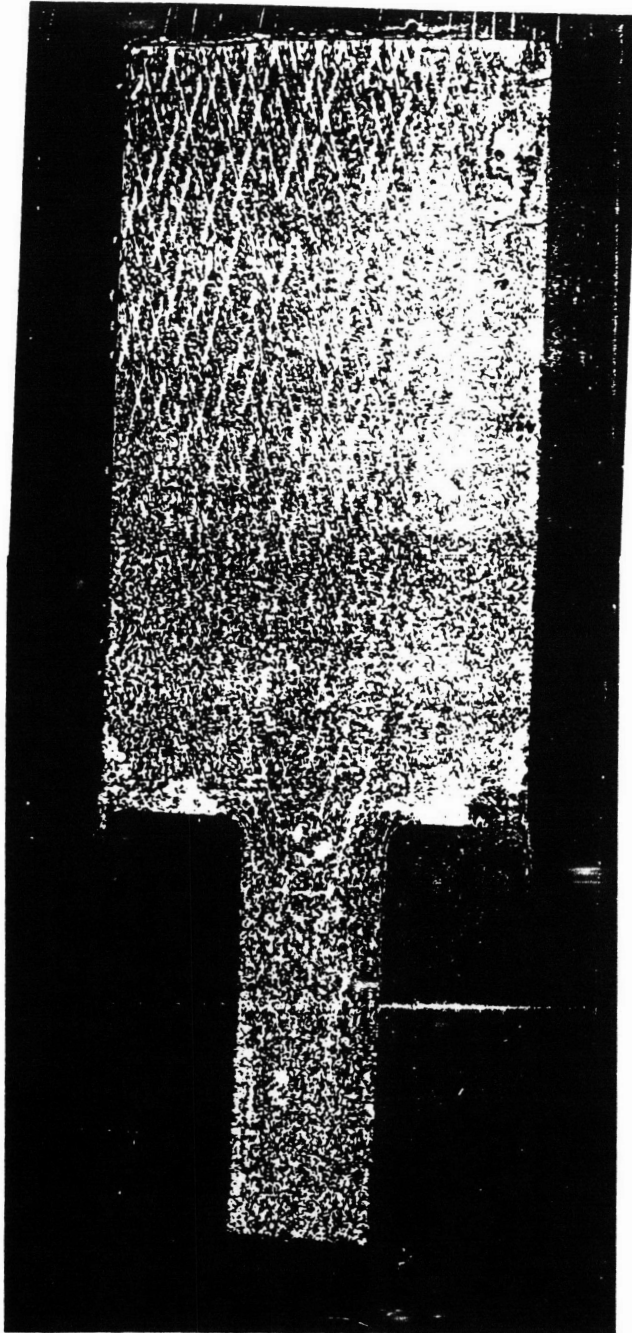
Fig.2-7. Optical Microscopy of a longitudinal cross-section of Al-4.5%Cu.
Magnification=6.5.

Fig.2-8. Optical Microscopy of a longitudinal cross-section of Al-4-5%Cu near
the end of the solidification process.   Magnification=12.
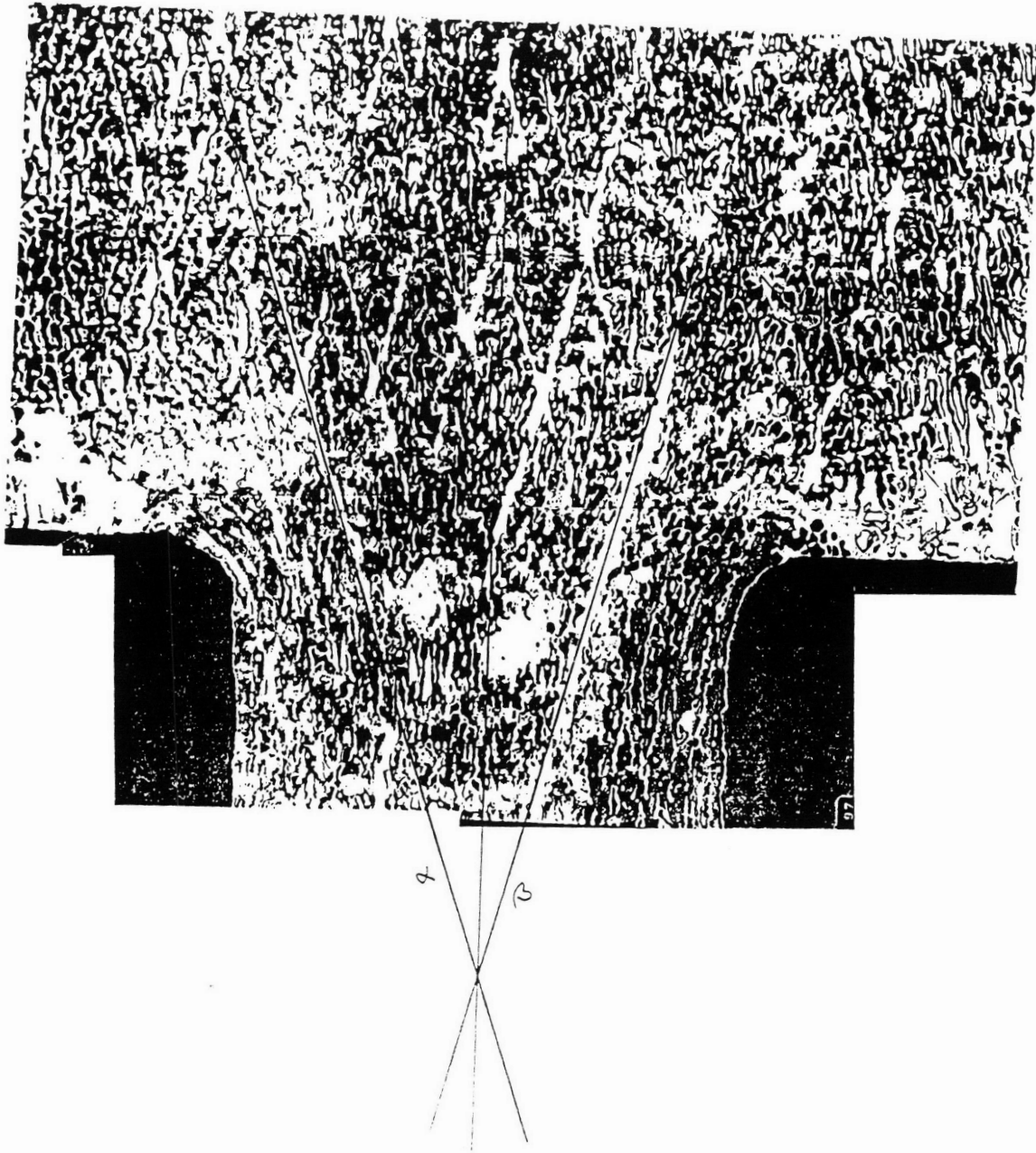
Fig.2-9. Dendritic structure of Al-4.5%Cu near mold corners.
Magnification=25.

castings indicate that one dendritic direction is dominant well before the solidification front reaches region of cross sectional change.

Figure 2-7 shows most clearly the formation of stray grains on the bottom part of the larger cross section. In this particular sample, it appears that secondary grains with two different compositions, as indicated by the white part on both sides of the cross-sectional increase and the black part at the outer edge of the right corner. The black part seems to be a contaminated part, whether by oxidation or a chemical reaction with the glue material in the mold. The white regions, however, appeared consistently in most of the samples, and could be assumed to be grains formed due to undercoolings in these regions during solidification. The general location and shape of these white areas were later compared to the solidification front pictures from the computational simulation runs.

When the increase in the cross-section occurs, the dendritic structure that has been growing primarily in one-dimension suddenly encounters a region where two primary growth directions are possible. At this point, the platform region has greater heat flux than the bulk of the casting, due to the heat flow to the mold. According to the principles of heat transport phenomena, this leads to accelerated local growth of dendrites, which means that any grains present in that region, whether by nucleation by undercooling or by dendrite remelting, will grow faster than the primary dendrite. In turn, this can lead to sizable defects due to stray grains or zebra grains (which are usually originated from stray grains, according to study by Schaefer et al. [6]).

The additional EBSP analysis of the defect parts revealed that, the degree of misorientation of zebra grains in actual cast parts from actual production lines, formed between the outer edge of the platform section and the center part of the casting, is on the order of 5 to 10 degrees. Figures 2-10 and 2-11 show the distribution of the
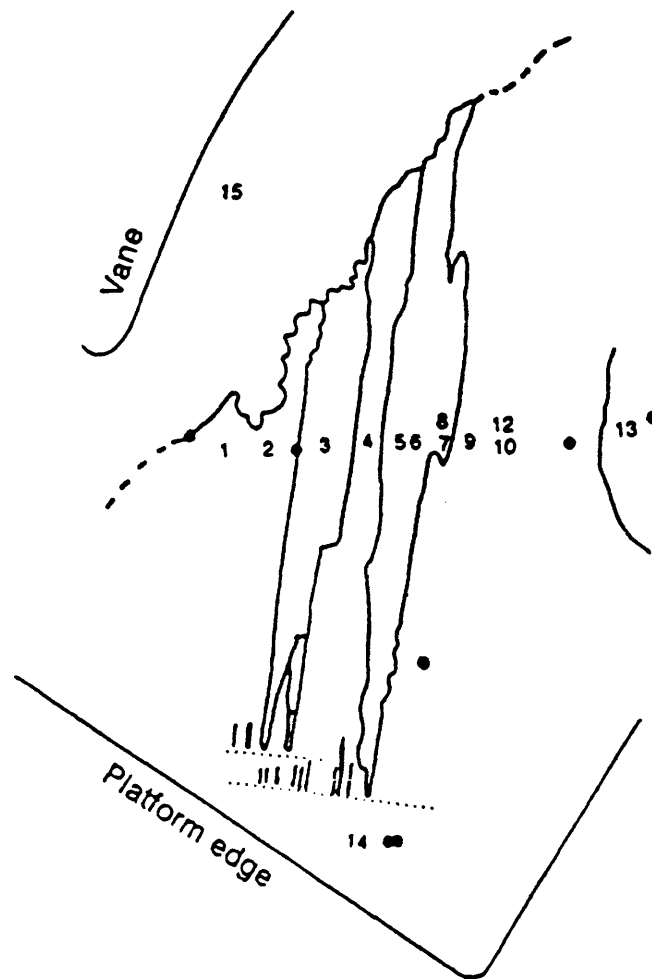
Fig.2-10. Locations of zebra grains on the platform of turbine blade. Misoriented
grains originate from sharply defined straight line (indicatd by dotted lines
here). The numbers correspond to points for electron channeling as shown
shown in Fig,2-11.
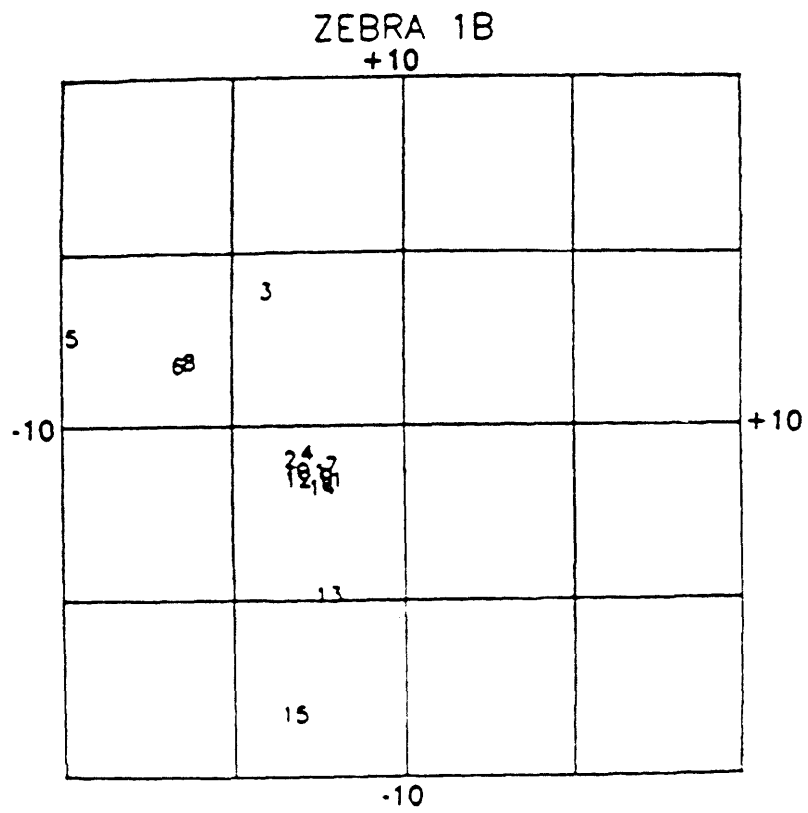
Fig.2-11. Degree of misorientation of zebra grains.   The normal to the platform
surface is at the center of the diagram.

misorientation angles of the zebra grains. The angle between the direction of the primary dendritic growth, denoted by point #15, and the direction normal to the surface of the platform, i.e., the overall growth direction, was found to be under 10 degrees. This was in accordance with the lower-end values of the misorientation angles from the experimental runs.

Table 2-1. Values of misorientation angle for points shown in Figure 2-6.

Point #	Misorientation angle (°)
1	6
2	5.6
3	5.5
4	5.3
5	5.8
6	5.7
7	5.3
8	4.9
9	4.7

The XRD results were consistent with those from the EBSP analysis. As seen in Table 2-1, the misorientation angle of these points ranges from 4° to 6°, generally decreasing as the points got closer to the center of the casting. Many of the points examined indicated presence of more than one crystallographic orientation by producing sets of double points that were very close in distance and thus very close in orientation. This is shown in the XRD photographs in Figure 2-12.

(b)

(a)
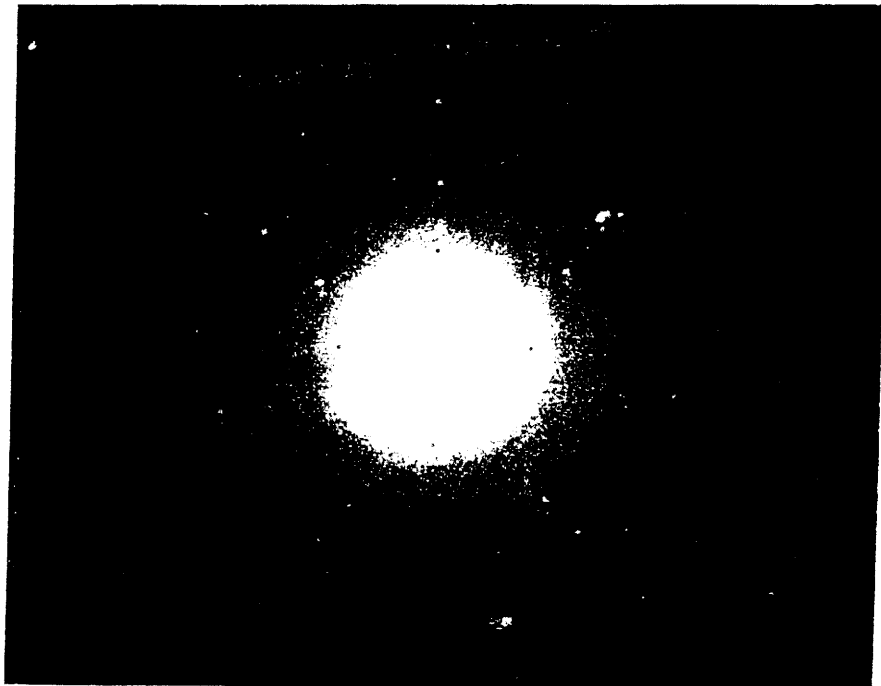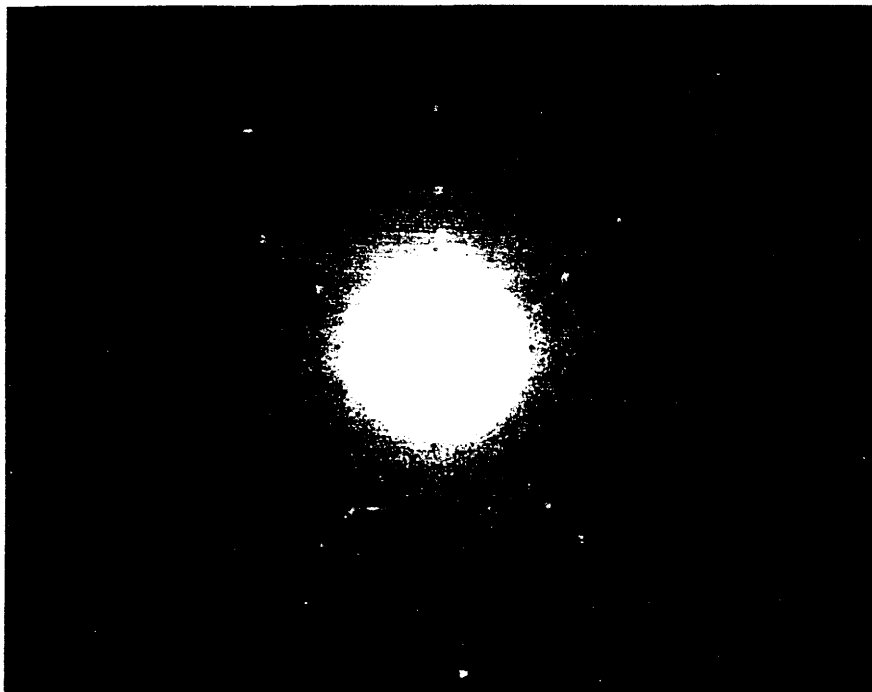
Fig.2-12. Laue diffraction pattern of points described in Fig. 2-6: (a) near #1;
(b) near #2.

2.6 Summary

Physical models of directional solidification of aerospace alloys were made with aluminum-4.5wt%copper alloy. The mold was made of alumina. Using a vertically moving furnace design, a small cylindrical geometry with cross-sectional change was produced in order to observe solidification patterns and possible defect formation in and around the platform region with greater cross-section than that of the bulk of the casting. The values of the processing parameters used in the physical model served as the basis for computational simulations.

Optical microscopy of a number of cast samples revealed presence of stray grains in the platform region, which was in good accordance with the presence of stray and zebra grains in the platform regions of defective turbine blade parts from actual manufacture lines. Although the actual parts were made of Inconel 718, and therefore possess characteristics which are different from those of the Al-Cu alloy, there was a good correlation between the two systems with respect to the orientation of the primary dendritic growth. Additional analysis of defective turbine blade parts showed that the zebra grains in the platform region had a small degree of misorientation relative to the primary dendritic growth direction.

3. ORDER OF MAGNITUDE ESTIMATES

3.1 Introduction

The assumption in this order of magnitude calculation is that there be no disturbances or turbulent effects during solidification of directional crystals. The main goals of this estimation are: to define the similarity between the conditions in the physical model (Al-Cu) and the prototype of actual system (Ni-based superalloy solidification in investment casting); and to estimate the main effect of different process conditions on promoting specific flow regimes.

Predicting analytically the outcome of any materials manufacturing process is quite complicated, involving many calculations and requiring knowledge of many material parameters and processing properties. Furthermore, when various units of measurement are used, it is difficult to draw accurate comparison between analyses having different sets of units or vastly different scales. To address this problem, the concept of dimensionless numbers was introduced. A dimensionless number is a parametric characteristic of a particular process, linking the processing conditions and the material(s) used by describing relationships among relevant parameters in a system to estimate possible regimes of operation.

A dimensionless number serves several purposes.

- By eliminating the need for any attention to units or scales (that is, between values of a dimensionless number, not within a formula), it enables easy and accurate comparison

between any set of similar systems that involve a dimensionless number even when the systems are not identical with respect to individual processing parameters.

- For a process involving multiple physical phenomena, dimensionless numbers indicate their relative importance, which, if any, can safely be ignored in process analysis.

- Regimes of behavior of a system, such as laminar versus turbulent flow can often be delivered for a given geometry by dimensionless numbers such as Reynolds number. Thus, when the value of a dimensionless number is obtained, the behavior of a system is determined with little further work.

- Very importantly, a dimensionless number calculation enables overall prediction of changes in the general behavior of a system, without need for further modelling. This is very useful especially when it is desired to change some materials processing parameters, since possible changes in parameters can be easily put in to the dimensionless number's formula. In turn, the magnitude of the dimensionless number allows one to estimate process parameter changes required to obtain desired behavior. Then the proposed changes can be analyzed in a computational model to observe specific effects of the changes parameters on the behavior of the system being modelled.

This type of asymptotic analysis was used in computational modelling (discussed in Chapter 4), when the initial set of processing parameters did not yield desired solidification patterns. First, it was recognized that the parameters governing the solidification pattern of a casting lie in the relative heat transfer values in different regions throughout the casting. Then dimensionless numbers that described heat transport phenomena were examined for processing parameters involved. Next, among the relevant processing parameters, those that could be varied in actual production, such as the initial temperature

profile, furnace wall temperature gradient, and heat transfer coefficient, were changed in subsequent simulations in order to obtain the desired solidification pattern.

On the other hand, a dimensionless number can also be used when there is a need to keep the behavior of a system constant, yet at the same time it is necessary to change one or more of the processing parameters involved. In this case, examining the dimensionless number that contains the changed parameters will specify whether the changes can be made without altering the general behavior of the system. That is, if a dimensionless number containing the changed parameters also has other parameters which can be controlled, then it is possible to keep the dimensionless numbers and the system's behavior constant even when individual parameters are changing. Otherwise, not all of the changes can be made without altering the behavior of the system.

The Reynolds number determines the nature of a flow, whether it is laminar, transitional, or turbulent, by examining the ratio of inertial forces to viscous forces. It is a function of dimension(L), velocity(u), density(ρ), and viscosity(μ) of a flow. The lower the value of the Reynolds number, the more laminar the flow. Its value increases with an increase in L, u, or ρ, and with decrease in μ, i.e. [7]:

$$Re = \frac{\rho u L}{\mu}$$
..... (3-1)

The Grashof number determines the contribution by free convection of heat in a flow by comparing the buoyancy forces and viscous forces involved. It is this number that illustrates the importance of the dimensional magnitudes of a system (characteristic length) in determining the nature of a flow. The parameters used are gravity(g), thermal expansion coefficient(β), density(ρ), characteristic length(L), temperature difference(ΔT), and kinematic viscosity(v) [8]:

$$Gr = \frac{g\beta\rho^2 L^3 \Delta T}{\mu^2} \qquad \ldots \ldots (3\text{-}2)$$

The Prandtl number compares momentum diffusivity with thermal diffusivity to determine the importance of forced and free convection of heat in a system. The parameters used are viscosity(μ), heat capacity(C_p), and thermal conductivity(k) [9].

$$Pr = \frac{\nu}{\alpha} = \frac{C_p \mu}{k} \qquad \ldots \ldots (3\text{-}3)$$

The Rayleigh number, the product of Grashof number and Prandtl number, examines the ratio of thermal convection to thermal conduction. The greater Rayleigh number, the more important convection in a system; the smaller, conduction [10].

$$Ra = Gr \cdot Pr = \frac{g\beta\rho^2 L^3 C_p \Delta T}{\mu k} \qquad \ldots \ldots (3\text{-}4)$$

The Nusselt number (thermal) examines the ratio of total heat transport to the contribution by heat conduction and incorporates heat transfer coefficient(h), characteristic length(L), and the fluid conductivity(k_{fluid}) [11].

$$Nu = \frac{hL}{k_{fluid}} \qquad \ldots \ldots (3\text{-}5)$$

This number will be discussed further in conjunction with h, heat transfer coefficient, in Section 3.5.

The Peclet number compares convective transport and diffusive transport, whether heat or mass. Here, solutal (mass) Peclet number is shown [12], with mass diffusion coefficient D, fluid velocity(v), and characteristic length R/2 (volume-to-surface area ratio for a cylinder). Thermal Peclet number replaces D with α, thermal diffusivity

$$Pe = \frac{vR}{2D} \qquad \ldots \ldots (3\text{-}6)$$

3.2 Sensitivity Analysis

Calculations were performed in order to establish ranges of temperature difference and geometric scale for possible types of flow regimes during solidification.

First, aluminum was examined. The values for various properties near the melting point were taken from literature [13]. Parameters such as density, thermal expansion coefficient, specific heat, thermal conductivity, and viscosity were used to calculate relevant dimensionless numbers for a system of given characteristic dimension (in the direction of the boundary layer) and temperature gradient (in the direction orthogonal to that of the characteristic dimension). Values for the properties of aluminum-copper that were used in obtaining such dimensionless numbers as Prandtl number, Grashof number, and Rayleigh number are shown in Table 3-1.

Table 3-1. Properties of molten aluminum-4.5%copper near melting point

density	$\rho = 2787 \ \mathrm{kg/m^3}$
viscosity	$\mu = 2 \times 10^{-3} \ \mathrm{kg/m \cdot s}$
kinematic viscosity	$\nu = 7.17 \times 10^{-7} \ \mathrm{m^2/s}$
specific heat	$C_p = 9.63 \times 10^{-1} \ \mathrm{KJ/Kg \cdot K}$
gravity	$g = 9.81 \ \mathrm{m/s^2}$
thermal expansion coefficient	$\beta = 1.27 \times 10^{-4} \ \mathrm{K^{-1}}$
thermal conductivity	$k = 1.67 \times 10^2 \ \mathrm{W/m \cdot K}$
thermal diffusivity	$\alpha = 6.22 \times 10^{-5} \ \mathrm{m^2/s}$
Prandtl number	$Pr = 1.15 \times 10^{-2}$
Grashof number	$Gr = 1.67 \times 10^9 \cdot \Delta T \cdot L^3$

Based on these numbers, values of Rayleigh number were obtained with the characteristic dimension and temperature gradient as variables. It was expected and found that the dimension has a greater influence on the value of the Rayleigh number than does the temperature gradient. Table 3-2 illustrates this point very clearly, as well as provides the combinations of these two parameters that would yield a transitional flow (the middle region of the table) and a fully-developed turbulent flow. A boundary layer flow, which characterizes the long and narrow geometry of the experimental setup, will have transitional fluid characteristics when the corresponding Rayleigh number is on the order of 10^5 or greater; for the value of 10^9 or higher, the flow will be fully turbulent. Because the physical dimensions of a casting plays a very important role in the variation of the Rayleigh number, intelligent interpretation of the data from experiments, whose scale is usually considerably smaller than an actual product, is essential.

dT (K)	L (m)									
	0.10	0.20	0.30	0.40	0.50	0.60	0.70	0.80	0.90	1.00
2	1.35E+05	1.08E+06	3.64E+06	8.64E+06	1.69E+07	2.92E+07	4.63E+07	6.91E+07	9.84E+07	1.35E+08
4	2.70E+05	2.16E+06	7.29E+06	1.73E+07	3.37E+07	5.83E+07	9.26E+07	1.38E+08	1.97E+08	2.70E+08
6	4.05E+05	3.24E+06	1.09E+07	2.59E+07	5.06E+07	8.75E+07	1.39E+08	2.07E+08	2.95E+08	4.05E+08
8	5.40E+05	4.32E+06	1.46E+07	3.46E+07	6.75E+07	1.17E+08	1.85E+08	2.76E+08	3.94E+08	5.40E+08
10	6.75E+05	5.40E+06	1.82E+07	4.32E+07	8.44E+07	1.46E+08	2.32E+08	3.46E+08	4.92E+08	6.75E+08
12	8.10E+05	6.48E+06	2.19E+07	5.18E+07	1.01E+08	1.75E+08	2.78E+08	4.15E+08	5.90E+08	8.10E+08
14	9.45E+05	7.56E+06	2.55E+07	6.05E+07	1.18E+08	2.04E+08	3.24E+08	4.84E+08	6.89E+08	9.45E+08
16	1.08E+06	8.64E+06	2.92E+07	6.91E+07	1.35E+08	2.33E+08	3.70E+08	5.53E+08	7.87E+08	1.08E+09
18	1.21E+06	9.72E+06	3.28E+07	7.78E+07	1.52E+08	2.62E+08	4.17E+08	6.22E+08	8.86E+08	1.21E+09
20	1.35E+06	1.08E+07	3.64E+07	8.64E+07	1.69E+08	2.92E+08	4.63E+08	6.91E+08	9.84E+08	1.35E+09
22	1.48E+06	1.19E+07	4.01E+07	9.50E+07	1.86E+08	3.21E+08	5.09E+08	7.60E+08	1.08E+09	1.48E+09
24	1.62E+06	1.30E+07	4.37E+07	1.04E+08	2.02E+08	3.50E+08	5.56E+08	8.29E+08	1.18E+09	1.62E+09
26	1.75E+06	1.40E+07	4.74E+07	1.12E+08	2.19E+08	3.79E+08	6.02E+08	8.99E+08	1.28E+09	1.75E+09
28	1.89E+06	1.51E+07	5.10E+07	1.21E+08	2.36E+08	4.08E+08	6.48E+08	9.68E+08	1.38E+09	1.89E+09
30	2.02E+06	1.62E+07	5.47E+07	1.30E+08	2.53E+08	4.37E+08	6.95E+08	1.04E+09	1.48E+09	2.02E+09
32	2.16E+06	1.73E+07	5.83E+07	1.38E+08	2.70E+08	4.67E+08	7.41E+08	1.11E+09	1.57E+09	2.16E+09
34	2.29E+06	1.84E+07	6.20E+07	1.47E+08	2.87E+08	4.96E+08	7.87E+08	1.18E+09	1.67E+09	2.29E+09
36	2.43E+06	1.94E+07	6.56E+07	1.56E+08	3.04E+08	5.25E+08	8.33E+08	1.24E+09	1.77E+09	2.43E+09
38	2.56E+06	2.05E+07	6.93E+07	1.64E+08	3.21E+08	5.54E+08	8.80E+08	1.31E+09	1.87E+09	2.56E+09
40	2.70E+06	2.16E+07	7.29E+07	1.73E+08	3.37E+08	5.83E+08	9.26E+08	1.38E+09	1.97E+09	2.70E+09

transitional

turbulent

L = characteristic dimension of system
dT = caracteristic temperature gradient

Table 3-2. Rayleigh number values for Al-4.5%Cu. The shaded are indicates turbulent regime as determined by the Rayleigh number.

50

Table 3-3 displays data for In718. Values for the properties used in the calculations were obtained mainly from A. Cezairliyan of NIST at Boulder, CO. [14] and from literature [15]:

Table 3-3. Properties of molten In718 near melting point

density	$\rho = 7320\ kg/m^3$
viscosity	$\mu = 4.5 \times 10^{-3}\ kg/m \cdot s$
kinematic viscosity	$v = 6.14 \times 10^{-7}\ m^2/s$
specific heat	$Cp = 1.0\ KJ/Kg \cdot K$
gravity	$g = 9.81\ m/s^2$
thermal expansion coefficient	$\beta = 1.36 \times 10^{-4}\ K^{-1}$
thermal conductivity	$k = 1.67 \times 10^1\ W/m \cdot K$
thermal diffusivity	$\alpha = 2.28 \times 10^{-6}\ m^2/s$
Prandtl number	$Pr = 2.69 \times 10^{-1}$
Grashof number	$Gr = 3.53 \times 10^9 \cdot \Delta T \cdot L^3$

The ranges of the characteristic dimension and temperature gradient that yield either transitional or turbulent flow patterns are particularly of interest here, for the comparison to the ranges for aluminum. By observing the values in both Table 3-1 (Al-Cu) and Table 3-3 (In718), it is clearly seen that, for similar process parameters, Inconel 718 is much more likely to exhibit transitional or turbulent characteristics than aluminum. Another interesting point is that it is much more difficult, for various reasons, to run an experiment using nickel-based alloys than aluminum-based ones. Therefore, it is important that proper adjustments be made to the results from any physical model using aluminum or aluminum-based alloys when drawing predictions either about the behavior of nickel-based alloys

51

L (m)

dT (K)	0.05	0.10	0.15	0.20	0.25	0.30	0.35	0.40	0.45
2	3.13E+06	2.50E+07	8.45E+07	2.00E+08	3.91E+08	6.76E+08	1.07E+09	1.60E+09	2.28E+09
4	6.26E+06	5.01E+07	1.69E+08	4.01E+08	7.82E+08	1.35E+09	2.15E+09	3.20E+09	4.56E+09
6	9.39E+06	7.51E+07	2.53E+08	6.01E+08	1.17E+09	2.03E+09	3.22E+09	4.81E+09	6.84E+09
8	1.25E+07	1.00E+08	3.38E+08	8.01E+08	1.56E+09	2.70E+09	4.29E+09	6.41E+09	9.12E+09
10	1.56E+07	1.25E+08	4.22E+08	1.00E+09	1.96E+09	3.38E+09	5.37E+09	8.01E+09	1.14E+10
12	1.88E+07	1.50E+08	5.07E+08	1.20E+09	2.35E+09	4.06E+09	6.44E+09	9.61E+09	1.37E+10
14	2.19E+07	1.75E+08	5.91E+08	1.40E+09	2.74E+09	4.73E+09	7.51E+09	1.12E+10	1.60E+10
16	2.50E+07	2.00E+08	6.76E+08	1.60E+09	3.13E+09	5.41E+09	8.59E+09	1.28E+10	1.82E+10
18	2.82E+07	2.25E+08	7.60E+08	1.80E+09	3.52E+09	6.08E+09	9.66E+09	1.44E+10	2.05E+10
20	3.13E+07	2.50E+08	8.45E+08	2.00E+09	3.91E+09	6.76E+09	1.07E+10	1.60E+10	2.28E+10
22	3.44E+07	2.75E+08	9.29E+08	2.20E+09	4.30E+09	7.43E+09	1.18E+10	1.76E+10	2.51E+10
24	3.75E+07	3.00E+08	1.01E+09	2.40E+09	4.69E+09	8.11E+09	1.29E+10	1.92E+10	2.74E+10
26	4.07E+07	3.25E+08	1.10E+09	2.60E+09	5.08E+09	8.79E+09	1.40E+10	2.08E+10	2.97E+10
28	4.38E+07	3.50E+08	1.18E+09	2.80E+09	5.48E+09	9.46E+09	1.50E+10	2.24E+10	3.19E+10
30	4.69E+07	3.75E+08	1.27E+09	3.00E+09	5.87E+09	1.01E+10	1.61E+10	2.40E+10	3.42E+10
32	5.01E+07	4.01E+08	1.35E+09	3.20E+09	6.26E+09	1.08E+10	1.72E+10	2.56E+10	3.65E+10
34	5.32E+07	4.26E+08	1.44E+09	3.40E+09	6.65E+09	1.15E+10	1.82E+10	2.72E+10	3.88E+10
36	5.63E+07	4.51E+08	1.52E+09	3.60E+09	7.04E+09	1.22E+10	1.93E+10	2.88E+10	4.11E+10
38	5.95E+07	4.76E+08	1.61E+09	3.80E+09	7.43E+09	1.28E+10	2.04E+10	3.04E+10	4.33E+10
40	6.26E+07	5.01E+08	1.69E+09	4.01E+09	7.82E+09	1.35E+10	2.15E+10	3.20E+10	4.56E+10

transitional

turbulent

L = characteristic dimension of system
dT = characteristic temperature gradient

Table 3-4. Rayleigh number values for Inconel 718. The shaded area indicates turbulent regime as determined by the Rayleigh number.

One factor to consider here is the difference in the level of tendency for a large temperature gradient between the two systems. Given a similar set of conditions such as the mold material, length scale and solidification speed, the larger conductivity of the Al-Cu system will make for a smaller temperature difference within the casting than that of Inconel 718, leading to faster solidification. Indeed, as discussed in Section 4.3, the overall solidification time for In718 in computational simulation is much larger than that of Al-Cu.

3.3   Undercoolings

Calculation was performed based on the paper by Rappaz et al. and using formulas in Kurz and Fisher in order to establish the magnitudes of primary dendrite trunk a..d secondary dendrite arm spacings and undercoolings. The main results from the calculation indicate that the secondary undercooling is greater in magnitude than primary undercooling and that the amount of the difference depends on the horizontal extension of the cross sectional area.

The radius at the tip of a dendrite can be written as [16][17]:

$$R = 2\pi \sqrt{\frac{\Gamma}{\sum m_i Gc_i - G}} \qquad \dots \dots (3\text{-}7)$$

where Γ is the Gibbs-Thomson coefficient, expressed as $\gamma/\Delta Sf$ vol, Gc is the solutal gradient, and G is the thermal gradient, obtained from the experimental setup. In Equation 3-7, the denominator of the fraction gives the degree of constitutional supercooling ϕ (units: K/m). R can also be written as[18]:

$$R = \frac{2DPe}{v} \qquad \ldots \ldots (3\text{-}8)$$

where v is the rate of the solidification front advancement and Pe is solutal Peclet number, expressed as[19]:

$$Pe = \pi \left(\frac{v\Gamma}{D\Delta T_0 k} \right)^{\frac{1}{2}} \cdot \qquad \ldots \ldots (3\text{-}9)$$

where ΔT_0, the solidification interval of the alloy, is the temperature difference of the liquidus and solidus lines at composition C_0, and can be determined from the phase diagram. Given, for a binary system such as Al-4.5%Cu, whose phase diagram is shown in Figure 3-1 [20],

$$T_L = T_m + mC_o \qquad \ldots \ldots (3\text{-}10)$$

and

$$T_S = T_m + \frac{m}{k}C_o \qquad \ldots \ldots (3\text{-}11)$$

where m is the slope of the liquidus and k is the partition coefficient,

$$\Delta T_0 = T_L - T_S = mC_o - \frac{m}{k}C_o = \frac{mC_o(k-1)}{k} \qquad \ldots \ldots (3\text{-}12)$$

and, using the values in Table 3-5, the estimated dendrite tip radius R for the process conditions in the physical model of Al-Cu is 1.03×10^{-5} m.

Table 3.5. Values for Al-4.5wt%Cu used in undercooling analysis.

D	3.03×10^{-9} m^2/s
Γ	2.40×10^{-7} Km
v	2.50×10^{-5} m/s
m	-2.78 K/wt%

k	0.143
Co	4.5 wt%
Ce	33.1 wt%
d	3.175×10^{-3} m
G	-6500 K/m
ΔT_0	74.97 K
t_f	461 s

The primary undercooling, ΔT_1, can be calculated using the following equation [21]:

$$\Delta T_1 = \Delta T_c = \Delta T_o \, k \, Iv(Pe) = mC_o \left(1 - \frac{1}{1 - Iv(Pe) \cdot (1-k)} \right) \quad (3\text{-}13)$$

where ΔT_c is the temperature difference due to solute diffusion, and Iv, the Ivantsov function, is defined for a paraboloid of revolution of the dendrite as [22]:

$$Iv(Pe) = Pe \cdot exp(Pe) \cdot E_1(Pe) \qquad \ldots \ldots (3\text{-}14)$$

E1 is the exponential integral function, which can be approximated as [23]:

$$E_1(Pe) \approx -0.577 - \ln(Pe) + \frac{4Pe}{Pe + 4} \qquad \ldots \ldots (3\text{-}15)$$

Iv(Pe) can also be written as [24]:

$$Iv(Pe) = \cfrac{Pe}{Pe + \cfrac{1}{1 + \cfrac{1}{Pe + \cfrac{2}{1 + \cfrac{2}{Pe + \cdots}}}}} \qquad \ldots \ldots (3\text{-}16)$$

56
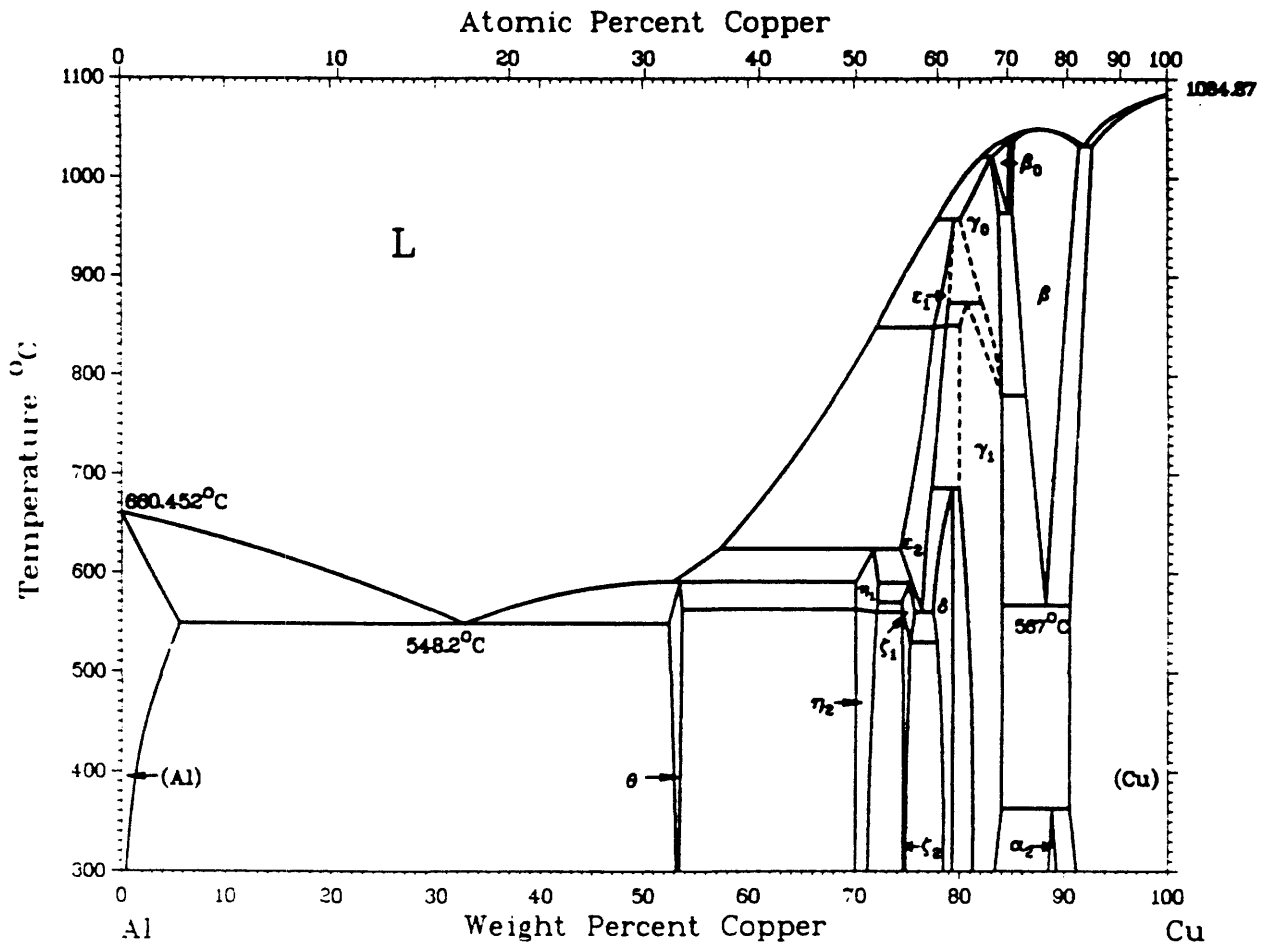
Fig.3-1. Binary phase diagram of Al-Cu.

and, for small Pe,

$$Iv(Pe) \cong Pe \qquad \qquad \dots \dots (3\text{-}17)$$

Then,

$$\Delta T_1 = mC_o\{1 - [1 + (1 - k)Pe]\} = mC_o(k - 1)Pe$$

$$= mC_o(k - 1)\pi\left(\frac{v\Gamma}{D\Delta T_o k}\right)^{\frac{1}{2}} \qquad \dots (3\text{-}18)$$

Again, using the values in Table 3-5, the value for the primary undercooling is estimated as $\Delta T_1 = 0.458$ K. Another way to write Eq. 3-18 for a given composition illustrates the relationship between ΔT_1 and v, the only variable in the equation for a given composition, as [25]:

$$v = A\Delta T_1^2 \qquad \qquad \dots \dots (3\text{-}19)$$

where A, the kinetic growth constant, is obtained from Eq. 3-18:

$$A = \frac{D\Delta T_o k}{\Gamma}\left(\frac{1}{mC_o(k - 1)\pi}\right)^2 \qquad \dots \dots (3\text{-}20)$$

Primary dendrite arm spacing, λ_1, can be obtained using the following equation [26]:

$$\lambda_1 = \sqrt{\frac{3\Delta T_o R}{G}} = M_1 \cdot G^{-\frac{1}{2}} \cdot v^{-\frac{1}{4}} \qquad \dots \dots (3\text{-}21)$$

where M_1 is a constant that incorporates everything except for the variables in the equation for a given composition:

$$M_1 = (6\pi)^{\frac{1}{2}}\left(\frac{D\Gamma\Delta T_o}{k}\right)^{\frac{1}{4}} \qquad \dots \dots (3\text{-}22)$$

Using Table 3-5, $\lambda_1 = 5.94 \times 10^{-4}$ m.

58

Knowing the primary undercooling and the lateral extension of the cross section, d, secondary undercooling can be calculated [27]:

$$\Delta T_2 = \left(\Delta T_1^3 + \frac{3 \cdot d \cdot G \cdot v}{A} \right)^{\frac{1}{3}} \qquad \ldots \ldots (3\text{-}23)$$

Table 3-5's values yield $\Delta T_2 = 2.356$ K.

This value is larger than that of the primary undercooling. Also, the ratio of secondary undercooling to primary undercooling increases with increasing d. If this value is greater than ΔT_n, undercooling sufficient for new nucleation, a new grain will form, which would be a defect within the context of directionally solidified alloys. Figure 3-2 shows the ΔT_2 values as a function of G with varying v and constant d (from Table 3-5). These three processing parameters have a same functional relationship with ΔT_2, the behavior pattern of the graphs will be the same as well for varying d with one of the other two parameters held constant.

λ_2, secondary dendrite arm spacing, can be calculated as follows [28]:

$$\lambda_2 = 5.5 \left(M_2 \cdot t_f \right)^{\frac{1}{3}} \qquad \ldots \ldots (3\text{-}24)$$

where M_2 is a constant that incorporates all the parameters in the equation except for t_f.

$$M_2 = -\frac{\Gamma \cdot D \cdot \ln\left(\dfrac{C_e}{C_o}\right)}{m(1-k)(C_e - C_o)} \qquad \ldots \ldots (3\text{-}25)$$

and t_f is local solidification time, given by [29]:

$$t_f = \frac{\Delta T'}{|\dot{T}|} = \frac{\Delta T'}{|G \cdot v|} \qquad \ldots \ldots (3\text{-}26)$$
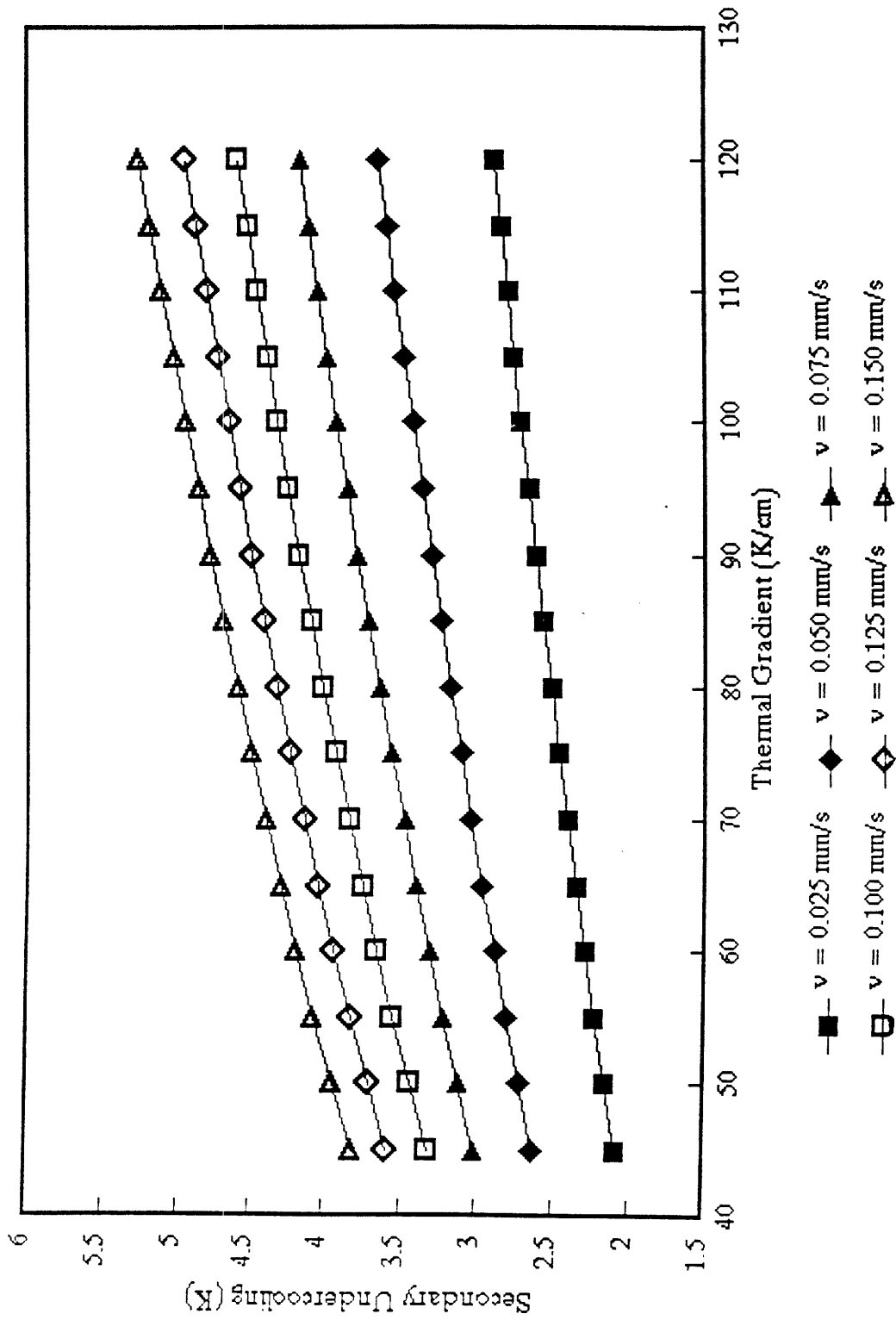
Fig.3-2. Secondary dendritic arm undercooling with varying temperature gradient and rate of solidification front advancement.

where $\Delta T'$, the tip-to-root temperature difference of dendrite, can be approximated as ΔT_0.

Again, using Table 3-5, $\lambda_2 = 1.18 \times 10^{-4}$ m, smaller than λ_1 but on the same order of magnitude. Examination of Equations 3-21 and 3-26 shows that the greater the temperature gradient and/or the solidification speed, the lower the local solidification time, which leads to smaller dendrite arm spacing. However, the undercooling values will increase with increasing v and G values (Eqns. 3-13 and 3-23). Therefore, varying either of these processing parameters should be done with these competing effects in mind.

3.4 Heat Transfer Coefficient

The next analysis involved calculation of the heat transfer coefficient between the molten metal and the mold wall. The heat transfer coefficient, while being a value depending on a particular system, can be theoretically obtained, given a set of conditions such as the nature of convection and the nature of the flow (boundary later or cavity flow). The basis for the calculation of the heat transfer coefficient comes from the following equation involving the dimensionless Nusselt number:

$$Nu = \frac{hL}{k_{fluid}} \qquad \ldots \ldots (3\text{-}5)$$

Given L and k, h can be obtained after the Nusselt number is calculated.

Since the magnitude of this number is crucial in deciding the nature of the flow, an accurate way of obtaining the number is an important step in turbulence studies. For processing conditions whose Grashof number is smaller than 10^8, the flow is assumed to be laminar, and the Nusselt number for natural convection from a vertical plate is [30]:

61

$$Nu = \frac{hL}{k_{fluid}} = \frac{0.508 Gr^{\frac{1}{4}} Pr^{\frac{1}{4}}}{\left(0.95 + Pr^{\frac{1}{4}}\right)} \qquad \dots\dots (3\text{-}27)$$

and for processing conditions whose Grashof number is larger than 10^8, the flow is

assumed to be turbulent, and the Nusselt number for natural convection from a vertical

plate is [31]:

$$Nu = \frac{hL}{k_{fluid}} = \frac{0.029 Gr^{\frac{2}{5}} Pr^{\frac{7}{15}}}{\left(1 + Pr^{\frac{2}{3}}\right)^{\frac{2}{5}}} \qquad \dots\dots (3\text{-}28)$$

It was found that there is a number of variations of those equations in literature that

are appropriate for particular situations [32]. Most of these equations, under identical or

equivalent processing conditions, yield values whose range lies within the general spectrum

of the Nusselt number values used in Tables 3.6 and 3.7.

Based on these equations, the heat transfer coefficient values of both aluminum-

copper alloy and In718 were calculated whose result appear in Tables 3-6 and 3-7.

Exhibiting a good agreement with Tables 3-4 and 3-5, they also show that for a given set of

processing conditions, In718 is much more likely to act in a turbulent manner than

aluminum.

A very interesting point to note pertains to the range of dimensionless numbers that

determine the nature of a fluid and the scale of geometry of a system. It is clear from

observing the equations for the Grashof number and the Rayleigh number that the tendency

dT (K)	0.10	0.20	0.30	0.40	0.50	0.60	0.70	0.80	0.90	1.00
2	2.53E+03	2.71E+03	2.93E+03	3.11E+03	3.25E+03	3.37E+03	3.48E+03	3.57E+03	3.65E+03	3.73E+03
4	3.01E+03	3.57E+03	3.87E+03	4.10E+03	4.29E+03	4.45E+03	4.59E+03	4.71E+03	4.82E+03	4.92E+03
6	3.33E+03	4.20E+03	4.55E+03	4.82E+03	5.04E+03	5.23E+03	5.39E+03	5.54E+03	5.67E+03	5.79E+03
8	3.58E+03	4.71E+03	5.11E+03	5.41E+03	5.66E+03	5.87E+03	6.05E+03	6.21E+03	6.36E+03	6.50E+03
10	3.78E+03	5.15E+03	5.58E+03	5.92E+03	6.19E+03	6.42E+03	6.62E+03	6.80E+03	6.96E+03	7.11E+03
12	3.96E+03	5.54E+03	6.01E+03	6.36E+03	6.65E+03	6.90E+03	7.12E+03	7.31E+03	7.48E+03	7.64E+03
14	4.11E+03	5.89E+03	6.39E+03	6.77E+03	7.08E+03	7.34E+03	7.57E+03	7.77E+03	7.96E+03	8.13E+03
16	4.25E+03	6.21E+03	6.74E+03	7.14E+03	7.46E+03	7.74E+03	7.98E+03	8.20E+03	8.40E+03	8.57E+03
18	4.38E+03	6.51E+03	7.06E+03	7.48E+03	7.82E+03	8.12E+03	8.37E+03	8.60E+03	8.80E+03	8.99E+03
20	4.50E+03	6.80E+03	7.37E+03	7.81E+03	8.16E+03	8.46E+03	8.73E+03	8.97E+03	9.18E+03	9.38E+03
22	4.60E+03	7.06E+03	7.66E+03	8.11E+03	8.48E+03	8.79E+03	9.07E+03	9.31E+03	9.54E+03	9.74E+03
24	4.71E+03	7.31E+03	7.93E+03	8.40E+03	8.78E+03	9.11E+03	9.39E+03	9.64E+03	9.87E+03	1.01E+04
26	6.57E+03	7.55E+03	8.18E+03	8.67E+03	9.06E+03	9.40E+03	9.70E+03	9.96E+03	1.02E+04	1.04E+04
28	6.77E+03	7.77E+03	8.43E+03	8.93E+03	9.34E+03	9.68E+03	9.99E+03	1.03E+04	1.05E+04	1.07E+04
30	6.96E+03	7.99E+03	8.67E+03	9.18E+03	9.60E+03	9.96E+03	1.03E+04	1.05E+04	1.08E+04	1.10E+04
32	7.14E+03	8.20E+03	8.89E+03	9.42E+03	9.85E+03	1.02E+04	1.05E+04	1.08E+04	1.11E+04	1.13E+04
34	7.31E+03	8.40E+03	9.11E+03	9.65E+03	1.01E+04	1.05E+04	1.08E+04	1.11E+04	1.14E+04	1.16E+04
36	7.48E+03	8.60E+03	9.32E+03	9.87E+03	1.03E+04	1.07E+04	1.10E+04	1.13E+04	1.16E+04	1.19E+04
38	7.65E+03	8.78E+03	9.53E+03	1.01E+04	1.06E+04	1.09E+04	1.13E+04	1.16E+04	1.19E+04	1.21E+04
40	7.81E+03	8.97E+03	9.72E+03	1.03E+04	1.08E+04	1.12E+04	1.15E+04	1.18E+04	1.21E+04	1.24E+04

L (m)

L = characteristic dimension of system
dT = characteristic temperature gradient

Table 3-6. Heat transfer coefficient values for Al-4.5%Cu. The shaded area indicates laminar regime.

dT (K)	L (m)									
	0.1	0.2	0.3	0.4	0.5	0.6	0.7	0.8	0.9	1
2	5.50E+03	6.32E+03	6.86E+03	7.26E+03	7.59E+03	7.88E+03	8.12E+03	8.34E+03	8.54E+03	8.72E+03
4	6.47E+03	7.44E+03	8.06E+03	8.54E+03	8.93E+03	9.26E+03	9.55E+03	9.81E+03	1.00E+04	1.03E+04
6	7.26E+03	8.34E+03	9.05E+03	9.58E+03	1.00E+04	1.04E+04	1.07E+04	1.10E+04	1.13E+04	1.15E+04
8	7.94E+03	9.12E+03	9.89E+03	1.05E+04	1.10E+04	1.14E+04	1.17E+04	1.20E+04	1.23E+04	1.26E+04
10	8.54E+03	9.81E+03	1.06E+04	1.13E+04	1.18E+04	1.22E+04	1.26E+04	1.29E+04	1.33E+04	1.35E+04
12	9.08E+03	1.04E+04	1.13E+04	1.20E+04	1.25E+04	1.30E+04	1.34E+04	1.38E+04	1.41E+04	1.44E+04
14	9.58E+03	1.10E+04	1.19E+04	1.26E+04	1.32E+04	1.37E+04	1.41E+04	1.45E+04	1.49E+04	1.52E+04
16	1.00E+04	1.15E+04	1.25E+04	1.33E+04	1.39E+04	1.44E+04	1.48E+04	1.52E+04	1.56E+04	1.59E+04
18	1.05E+04	1.20E+04	1.31E+04	1.38E+04	1.45E+04	1.50E+04	1.55E+04	1.59E+04	1.63E+04	1.66E+04
20	1.09E+04	1.25E+04	1.36E+04	1.44E+04	1.50E+04	1.56E+04	1.61E+04	1.65E+04	1.69E+04	1.72E+04
22	1.13E+04	1.29E+04	1.40E+04	1.49E+04	1.55E+04	1.61E+04	1.66E+04	1.71E+04	1.75E+04	1.79E+04
24	1.16E+04	1.34E+04	1.45E+04	1.54E+04	1.61E+04	1.67E+04	1.72E+04	1.76E+04	1.81E+04	1.84E+04
26	1.20E+04	1.38E+04	1.49E+04	1.58E+04	1.65E+04	1.72E+04	1.77E+04	1.82E+04	1.86E+04	1.90E+04
28	1.23E+04	1.42E+04	1.53E+04	1.63E+04	1.70E+04	1.76E+04	1.82E+04	1.87E+04	1.91E+04	1.95E+04
30	1.26E+04	1.45E+04	1.58E+04	1.67E+04	1.74E+04	1.81E+04	1.87E+04	1.92E+04	1.96E+04	2.00E+04
32	1.30E+04	1.49E+04	1.61E+04	1.71E+04	1.79E+04	1.85E+04	1.91E+04	1.96E+04	2.01E+04	2.05E+04
34	1.33E+04	1.52E+04	1.65E+04	1.75E+04	1.83E+04	1.90E+04	1.96E+04	2.01E+04	2.06E+04	2.10E+04
36	1.35E+04	1.56E+04	1.69E+04	1.79E+04	1.87E+04	1.94E+04	2.00E+04	2.05E+04	2.10E+04	2.15E+04
38	1.38E+04	1.59E+04	1.72E+04	1.82E+04	1.91E+04	1.98E+04	2.04E+04	2.10E+04	2.15E+04	2.19E+04
40	1.41E+04	1.62E+04	1.76E+04	1.86E+04	1.94E+04	2.02E+04	2.08E+04	2.14E+04	2.19E+04	2.23E+04

L = characteristic dimension of system
dT = characteristic temperature gradient

Table 3-7. Heat transfer coefficient values for Inconel 718.

64

of a flow to behave turbulently, i.e., the values of the numbers, increases as the third power of the characteristic dimension of its geometry. However, merely designing the geometry of a system on a smaller scale in order to avoid turbulence may not succeed. A change in the scale of the geometry of a system may be enough to change the nature of the flow, for example, from a cavity flow to a boundary layer flow. A such change in the nature of the flow will in turn result in the change of the range of the dimensionless numbers that determine the degree of turbulence in a flow. For example, a cavity flow is generally considered to be turbulent only for the Rayleigh number greater than 10^9 and/or the Grashof number greater than 10^8.

However, for a boundary layer flow, whose characteristic dimension is frequently much smaller than that of a cavity flow, the threshold values of the dimensionless numbers are significantly lower. Because of the interdependence of the processing conditions and relevant equations, it is very important to consider all factors that contribute to the nature of a flow when optimizing a set of processing conditions.

3.5 Radiation

The main reason that radiative heat transfer becomes important at high temperatures is that, although it exists at all temperature range, the relationship between the contribution by radiation increasing as temperature to the fourth power (as shown in Eq. 3-29), making its effect increase dramatically with increasing temperature. Generally, at temperatures above 500°C, radiation is considered to be very important, becoming more important as temperature increases, sometimes to the point of making contributions by all the other heat transfer mechanisms negligible.

For in718, which solidifies at temperatures of about 640 K to 830 K above 500°C, radiation is certainly extremely important. In order to serve as a means of verification of computational modelling and as an aid in determining the relative effect of radiation as compared to convection and/or conduction, calculation of overall solidification time for In718 was performed, first modelling the system as being mostly governed by radiation. Then the time scale thus obtained was compared to that of an actual production with comparable scale of characteristic dimension.

In this calculation, the mold was assumed to have uniform cross section. Starting from the equation for radiative heat transfer [34],

$$q = \varepsilon\sigma\left(T^4 - T_w^4\right) \qquad \dots \dots (3\text{-}29)$$

which yields

$$A \cdot q \cong \left(V\rho C_p\right)\frac{dT}{dt} \qquad \dots \dots (3\text{-}30)$$

$$\varepsilon\sigma\left(T^4 - T_w^4\right) = \frac{V}{A}\rho C_p \frac{dT}{dt} \qquad \dots \dots (3\text{-}31)$$

$$\int \frac{\varepsilon\sigma}{\rho C_p} \frac{A}{V} dT = \int \frac{dT}{T^4 - T_w^4} \qquad \dots \dots (3\text{-}32)$$

The time needed for Inconel 718 to go from a completely molten state to a solid state can be calculated from above equations, assuming the radiation is the main method of heat transfer. Calculation done in this manner showed that even ignoring the wall temperature, i.e., setting it to 0 K, the total time for solidification was on the order of hours. (For a

cylinder with 1 inch diameter and 2.5 inch height it takes about 8 hours to go from 1530 K to 1370 K with 0 K wall temperature.)

The emissivity values of the inner furnace wall and the outer mold wall were obtained initially by literature search [33] which provided a starting point. After that the emissivity values were adjusted and varied in order to observe their effects on the solidification patterns. In the final models whose simulations are discussed in Chapter 4, temperature-dependent emissivity values were used for the mold and the furnace walls. The emissivity values range from 0.4 to 0.7 for the temperature range of 400 to 1800 K.

While this generally agrees with the simulation results (Section 4.3) where it takes about 10 hours for the lower part of the mold to be solidified, it does not correspond to the actual time scale observed in the manufacturing process, which is at least an order of magnitude smaller. This suggests the following. First, radiation may not be as dominant a method of heat transfer even at this high range of temperature, meaning, other methods of heat transfer should be considered at the same time. There may be a sizable amount of conduction and/or convection that needs to be taken into account. Second, effective emissivity, reflectivity, and radiativity of surfaces involved may be considerably different from the values used in the analysis and modelling. Third, the calculated values for heat transfer coefficient between In718 and the mold may be different from the actual values.

3.6 Summary

In this chapter, the concept of dimensionless numbers was discussed, with specific descriptions of those relevant to the physical and mathematical modelling of this thesis. The Rayleigh number determines the nature of a flow in a system. It has a linear

functional relationship with the temperature difference within a casting, and is proportional to the cube of the characteristic dimension of a casting system. The values of the Rayleigh number were estimated for Al-4.5%Cu alloy and Inconel 718 with varying temperature difference and characteristic length.

Concentrating on the region of a cross-sectional increase, which is a typical geometric configuration for turbine blades, calculations were performed to estimate the degrees of primary and secondary undercoolings and primary and secondary dendrite spacings around the mold corner for the system used in the physical model. A large enough value of secondary undercooling can cause nucleation in the platform region, which in turn can lead to grain defects. A big increase in the cross-section, a large thermal gradient, and a high solidification front speed all increase the secondary undercooling.

The ranges of the value for the heat transfer coefficient were obtained using equations involving the Nusselt number. It was found that, for a given set of temperature difference and the characteristic length, In718 has a greater tendency toward turbulence than does Al-4.5%Cu. In addition, radiative heat transfer was discussed, with an estimation of overall solidification time due to radiation for In718.

The ranges of values obtained for the physical model were examined for any accordance with the solidification pattern results of the physical model. The values obtained for both Al-Cu system and In718 served as the basis of some input data for computer simulation program (discussed in Chapter 4). In addition, the solidification time calculation using the radiative heat transfer equation was compared to the time scale of simulated solidification runs for In718 (also discussed in Chapter 4).

4. COMPUTATIONAL MODELLING

4.1 Introduction

Although order-of-magnitude analysis provides an engineer with important insights into the nature of a process, it is very limited in its ability to make detailed predictions about a process, particularly where physical phenomena are as complex as heat transfer, and nonlinear as fluid flow. For these details, we turn to the mathematical engine of a computer. Over the last couple of decades, computer hardware and software have developed to the point where we can perform "numerical experiments" in which we solve for the full distributions of temperature, fluid flow and solidification front motion throughout an entire casting. Here we take advantage of these numerical experiments to advance the design of directional solidification casting furnaces.

In this study, such numerical experiments were first performed using the same parameters as were used in physical experiments, in order to verify their accuracy. Next, parameters were modified in a number of ways, including the geometry of the mold and casting and the temperature distribution in the furnace wall.

This chapter presents an outline of the simulation procedure using the ProCAST™ software package, and present results of the numerical experiments thus performed.

4.2 Simulation

The ProCAST™ software used here is divided into four modules: Mesh, in which the user defines the problem geometry and discretization; PreCAST, which involves the entry of material properties and other casting parameters; ProCAST, which numerically solves the problem; and ViewCAST, which assists the user in examining the results [35].

Within the module Mesh, the general procedure for defining the problem geometry is as follows. First, the user enters the range of the physical domain of the problem. This includes not only the size of the casting and the mold, but in the case of directional solidification, the range of motion of the mold relative to the furnace walls. Next, the geometry of the system is drawn, with lines representing interfaces between different materials such as the molten casting and the mold. Lines are also drawn to divide a material into various sections, each of which can have different mesh spacings, which allows for regions of interest to have higher resolution than less important regions during the calculation. Finally, the sections are actually meshed according to the user's specifications for mesh spacing. This part of the procedure can be omitted if the user imports a mesh from another program with capacity for more complex shapes (such as Patran, by PDA Engineering).

The geometry used for the analysis in this paper was axisymmetric, so that the specified 2-D geometry is effectively rotated about the axis of symmetry. This means that the figures generated by the software represent one half of a cross section of the system through the axis of symmetry. The mold shape programmed and simulated here closely resembles the actual physical setup discussed in Chapter 2, with slight variations on the placement of the cross sectional increase and the overall diameter of the mold. Figure 4-1 shows the casting and mold, with and without the meshing. The left part of the figure is
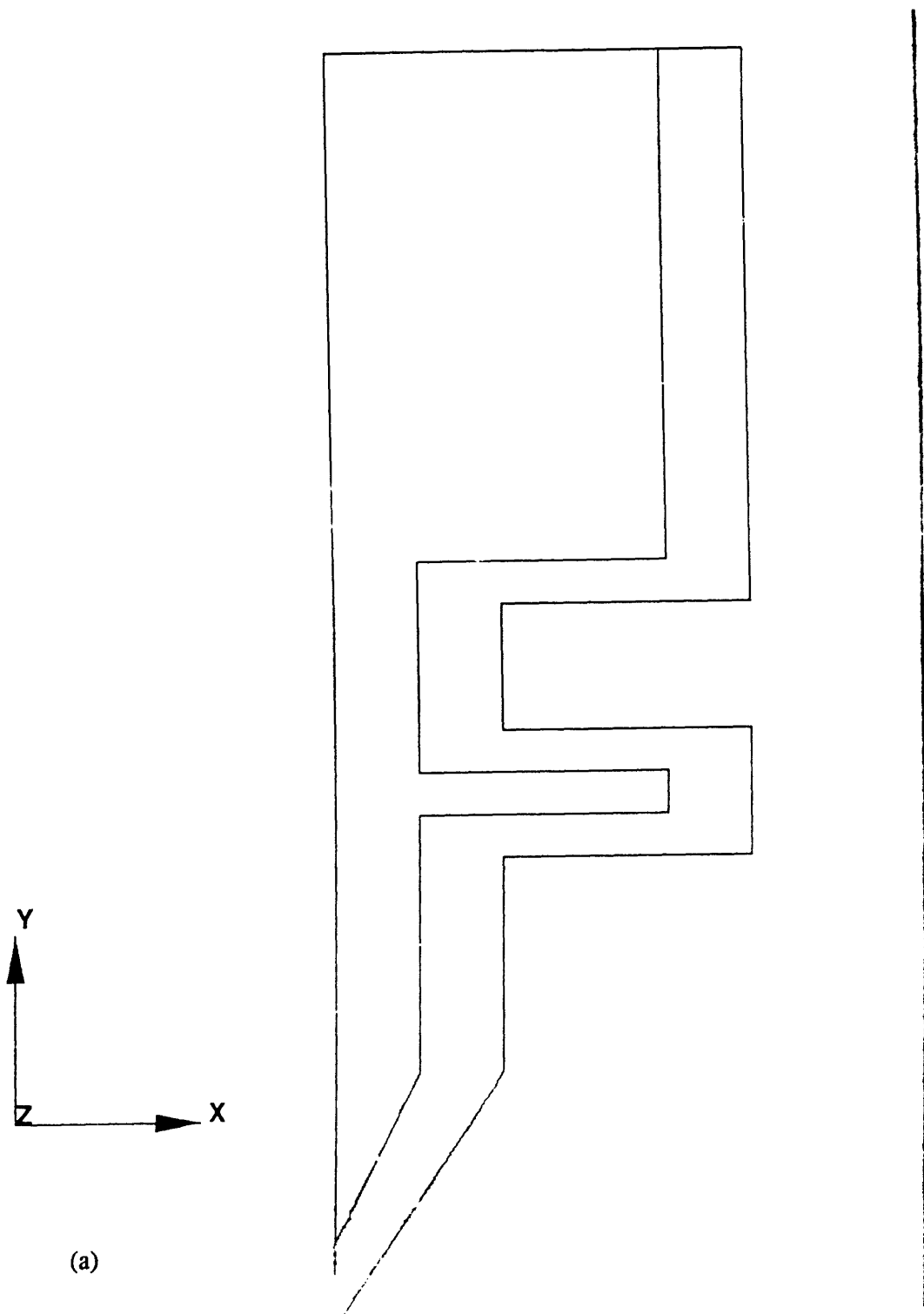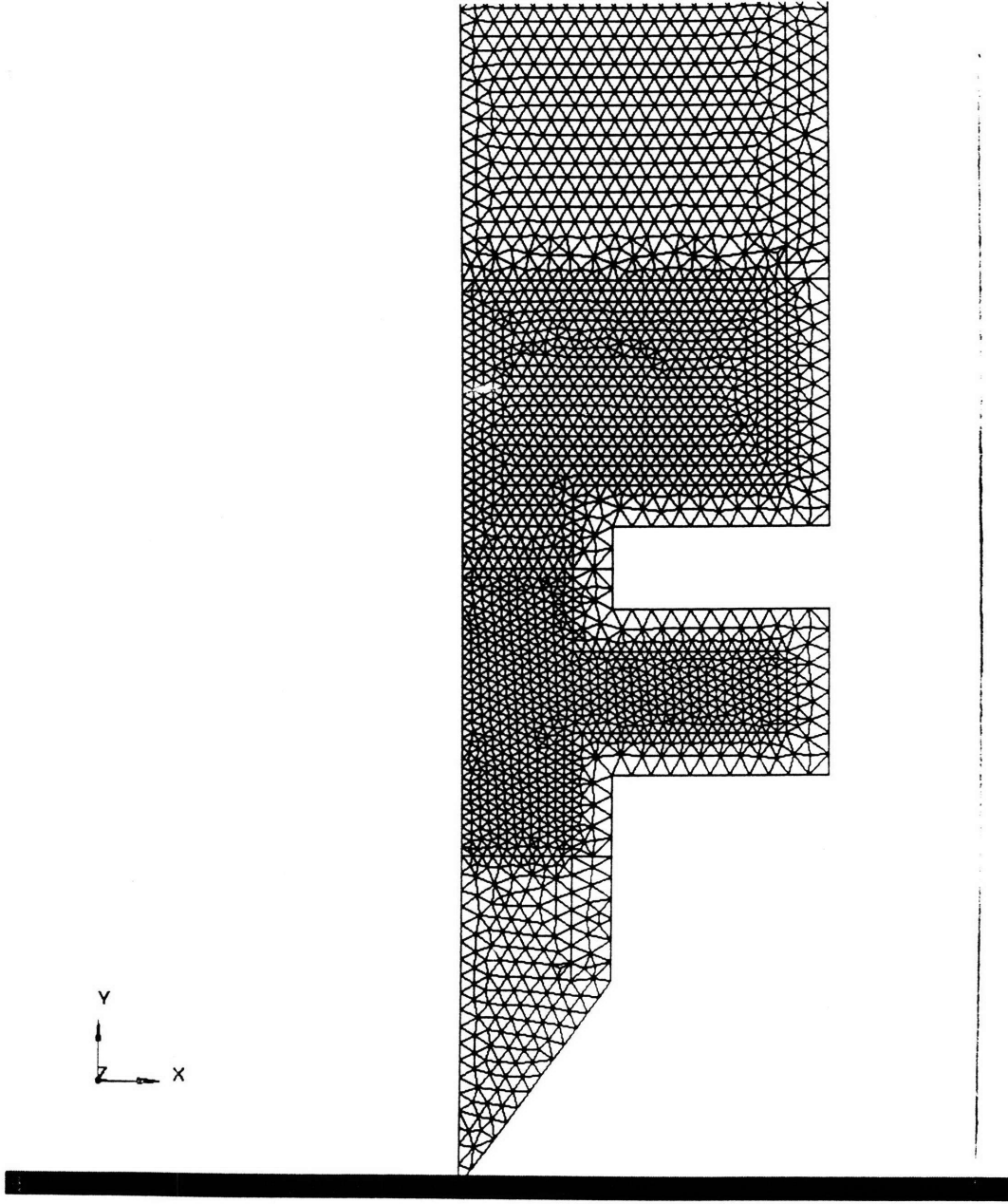
Fig.4-1. Schematic of casting geometry used in computational modelling.
(a)without mesh; (b)with mesh.

71

(b)

the casting (molten metal) and the right part corresponds to the mold. The more finely meshed regions in the casting part, such as the change in the cross-section, are the main points of interest in the casting. The vertical line to the right of the mold is the enclosure, which represents the inner furnace wall.

It is very important to create good geometry and the meshings, since after the Mesh module is completed, the program records the whole setup in a file, which serves as the reference basis for subsequent data input such as temperature, pressure, emissivity, and velocity, in the PreCAST module. Any changes in the geometry or mesh size will necessitate re-programming of some of the input values in PreCAST.

In PreCAST, the first step is to input the heat transfer coefficient values (h) at interfaces. This can be programmed as a constant or as a function of either time or temperature. Two ways of assigning h were used in this analysis: the constant h approach with several different values ranging from $2x10^3$ to $5x10^3$ for Al-Cu, and from $5x10^3$ to $1x10^4$ for In718; and the temperature-dependent h method, whose values were based on the sensitivity analysis in Chapter 3 (Tables 3-6 and 3-7). In later simulations, the heat transfer coefficient values were modified in order to examine any changes in the solidification pattern due to changes in the h values.

The second step is to assign materials to the sections and provide relevant materials properties. In this analysis, the relevant properties were: liquidus and solidus temperatures, density, heat capacity, viscosity (molten metal only), fraction solid, thermal conductivity, and latent heat (molten metal only). Of these, density, heat capacity, viscosity, and thermal conductivity can be either constant or a linear or quadratic function of temperature. In addition, for fraction solid, there are standard models such as Scheil equation that are pre-programmed and can be modified if necessary.

ProCAST comes with pre-programmed properties of a number of standard materials, but a useful feature of this software is that the user can either input data for a new material or change properties of an existing one by copying some of the pre-programmed values into a new entry. Each of the pre-programmed values came with a cited source for verification. Once a set of data for a material is created and saved, this can be used not only by the creator of the entry but by everyone, thus eliminating the need to input data each time a simulation of a system is carried out. In this analysis, Al-Cu alloy properties were either taken from literature or slightly modified versions of pre-programmed Al-5.0%Cu data in the software [36]. For In718, the values were taken from A. Cezairliyan's data [37]. For both materials, the Scheil equation was used to determine the fraction solid as a function of temperature. For the mold material alumina, most of the properties were taken from pre-programmed data, with the exception of density and temperature- and porosity-dependent thermal conductivity, which were taken from literature[38].

The third step is to set the boundary conditions on the system. This is difficult, since these conditions are not as easily determined as the materials properties. The necessary conditions were temperature (constant or time-dependent), ambient temperature or view factors, emissivity, velocity, and pressure. Both systems were simulated with and without the effect of radiation. (With radiation turned off, convection was considered the primary mode of heat transfer.)

For Al-Cu, whose mushy temperature range goes from 548°C to 644°C, both radiation and convection were considered important. For In718, which solidifies at a much higher temperature of 1144°C to 1334°C, the effect of radiation was assumed to be much more pronounced. The temperature-dependent emissivity values for the mold were taken from literature [39], and the In718 data were provided by A. Cezairliyan [40].

It should be noted that because some of the data in the PreCAST stage are stored in the permanent data bank of the software and can be re-used in subsequent runs by other users (on the same host machine), it is important not only to enter accurate values but also to label them in a way that makes them recognizable to other users. The more materials data there are in the data bank, the easier it becomes to prepare for a simulation.

A number of characteristic differences distinguish Al-4.5%Cu alloy from Inconel 718. The conductivity of the Al-Cu alloy is greater than that of the nickel alloy by more than an order of magnitude in their respective ranges of temperature for the solid state, while Inconel 718 has higher density (by a factor of 2 to 3) and higher viscosity (by a factor of app. 2). The specific heat is about the same for both alloys. Finally, the temperature range (liquidus to solidus) for the solidification of Inconel 718 is much higher than that for the Al-Cu, by about 400 K. These differences suggest that, given a set of equivalent processing conditions such as the mold material and geometry and the speed of the vertical movement of the casting with respect to the furnace, Inconel 718 would flow more slowly due to its higher viscosity and there would be more of a temperature gradient in its molten state due to its lower conductivity.

A note should also be made about the changes in the materials property values for alumina, the mold material, for Al-Cu and In718. Between the solidification temperature ranges for Al-Cu and Inconel 718, the mold's conductivity drops by almost 40 %, and the emissivity decreases by about 20 %. Another difference between the processes for the two alloys is in the heat transfer coefficients due to both the different values of the relevant dimensionless numbers and the difference in the working temperature ranges. The difference in temperature ranges will also change greatly the amount of radiative heat generated by the furnace and the mold walls.

75

The next step involves radiation calculation. It requires data on enclosure, representing the inner furnace walls in the experimental setup. This enclosure was drawn in the geometry file at the same time as the casting, and can be used even when radiation is not an important method of heat transfer, i.e., at low temperatures. The enclosure is divided into sections, so that each section can have different values of emissivity (temperature-dependent), temperature, and velocity. The vertical movement of the enclosure with respect to the casting can be represented either by making the temperature of each section change with time, by providing an upward velocity, or both.

For Al-Cu, simulations were first made with the enclosure exactly corresponding to the actual furnace in terms of temperature range, temperature gradient values (whose distribution varied depending on the maximum temperature, as discussed in Section 2.3), and the speed of vertical movement with respect to the casting. In subsequent runs, different temperature profiles were put in to observe changes in the solidification pattern.

Initial runs with In718 incorporated temperature gradient values similar to those for Al-Cu, both for the mold and the enclosure, with appropriate adjustments in the temperature ranges. Subsequently, variations were introduced in temperature ranges gradients, for a large number of simulations, in order to observe effects of different processing parameters on solidification pattern. In later runs of In718, the mold geometry was modified from having an angled bottom to a flat bottom.

The final step in PreCAST is the entry of run parameters. These include selection of calculation methods, size of time step, number of time steps, and selection of output data such as temperature profile, heat flux, solid fraction, and pressure. The contents of this step, though part of PreCAST, is stored in a separate file that can be edited without having to re-run all of this module. With every selection made here, it is important to balance

between accuracy of the output and speed of the simulation process so as to make the whole simulation process accessible and useful at the same time. Time step sizes were varied under identical processing conditions to observe to determine the upper limit of the time step size for accurate enough output. Also, time step intervals at which the calculations were updated were varied.

The ProCAST module is run next to actually solve the problem, and it generates output files which can be viewed using ViewCAST. The time required for each run, though depending greatly on the run parameters of the program, was usually on the order of hours. By examining the evolution of isotherms in temperature profiles and the fraction solid profiles, the position of the solidification front and the thickness of the mushy zone can be determined. The heat flux profile provides information on heat dissipation distribution.

4.3 Results and Discussion

It was found through many simulation runs that, by modifying processing parameters, it is possible to cause changes in the solidification pattern of directionally solidified casting, especially in the region of cross-sectional change. Specifically, changes in the values used, such as the heat transfer coefficient, initial temperature distribution, and temperature gradients in the enclosure, can lead to changes in the advancement pattern of the solidification front. Modifying parameter values also leads to changes in total solidification time and the heat flux distribution pattern within the casting.

Patterns of solidification front advancement fell into two categories depending on the values of variable processing parameters used. An example of one category is shown

in Figure 4-2 for Al-Cu, where a secondary solidification front forms at the outer edge of the platform growing laterally inward before the primary solidification front from below reaches the platform. This will increase the chances for formation of separate grains from the outer edge of the platform, growing inward. This solidification front advancement was in good agreement with the pattern suggested by the microscopy pictures from the physical modelling, in which secondary grains formed in corners of the increased cross-section.

The other case, as shown in Figure 4-3, also for Al-Cu, is where a single solidification front advances upward through the main part and outward laterally in the platform. With this solidification front advancement pattern, there is a much lower probability of formation of separate grains around the corners of increased cross-section. It is therefore the preferred solidification pattern over the first, although it may lead to porosity near the outer edges of the platform. The difference between the two types of solidification patterns is caused by differences in the processing parameters such as the heat transfer coefficient and the initial temperature gradient within the casting (metal and the mold) and in the enclosure.

Using the same geometry as for Al-Cu in simulating the solidification of Inconel 718 mainly resulted in the first type of solidification pattern, i.e., the formation of a second solidification front from the outer end of the platform region, as shown in Figure 4-4. Varying processing parameters as in the Al-Cu simulation did little to change the overall pattern significantly. This led to simulation runs with a change in the bottom shape of the mold geometry in the simulation, from an angled tip to a flat one. With this change in geometry of the mold, it was possible to generate a solidification pattern that advanced as one line, going outward in the platform, shown in Figure 4-5. However, this method slowed down the total solidification time even further.
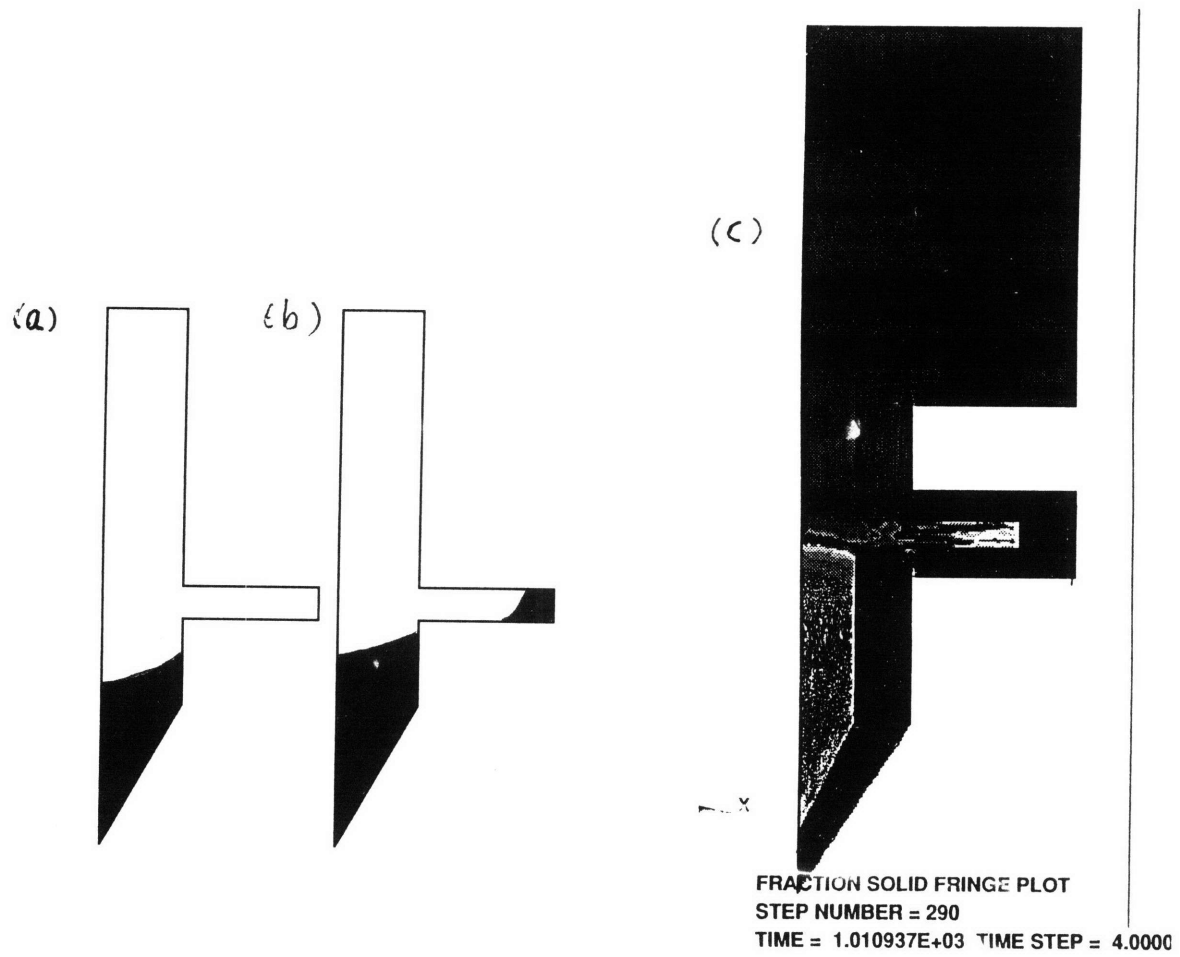
(a)

(b)

(c)

FRACTION SOLID FRINGE PLOT
STEP NUMBER = 290
TIME = 1.010937E+03 TIME STEP = 4.0000

Fig.4-2. Solidification pattern of Al-4.5%Cu type 1. (a) and (b) are schematics;
(c) fraction solid plot.

FRACTION SOLID FRINGE PLOT
STEP NUMBER = 140

FRACTION SOLID FRINGE PLOT
STEP NUMBER = 180

FRACTION SOLID FRINGE PLOT
STEP NUMBER = 220

FRACTION SOLID FRINGE PLOT
STEP NUMBER = 260

FRACTION SOLID FRINGE PLOT
STEP NUMBER = 300

FRACTION SOLID FRINGE PLOT
STEP NUMBER = 340

FRACTION SOLID FRINGE PLOT
STEP NUMBER = 380

FRACTION SOLID FRINGE PLOT
STEP NUMBER = 420
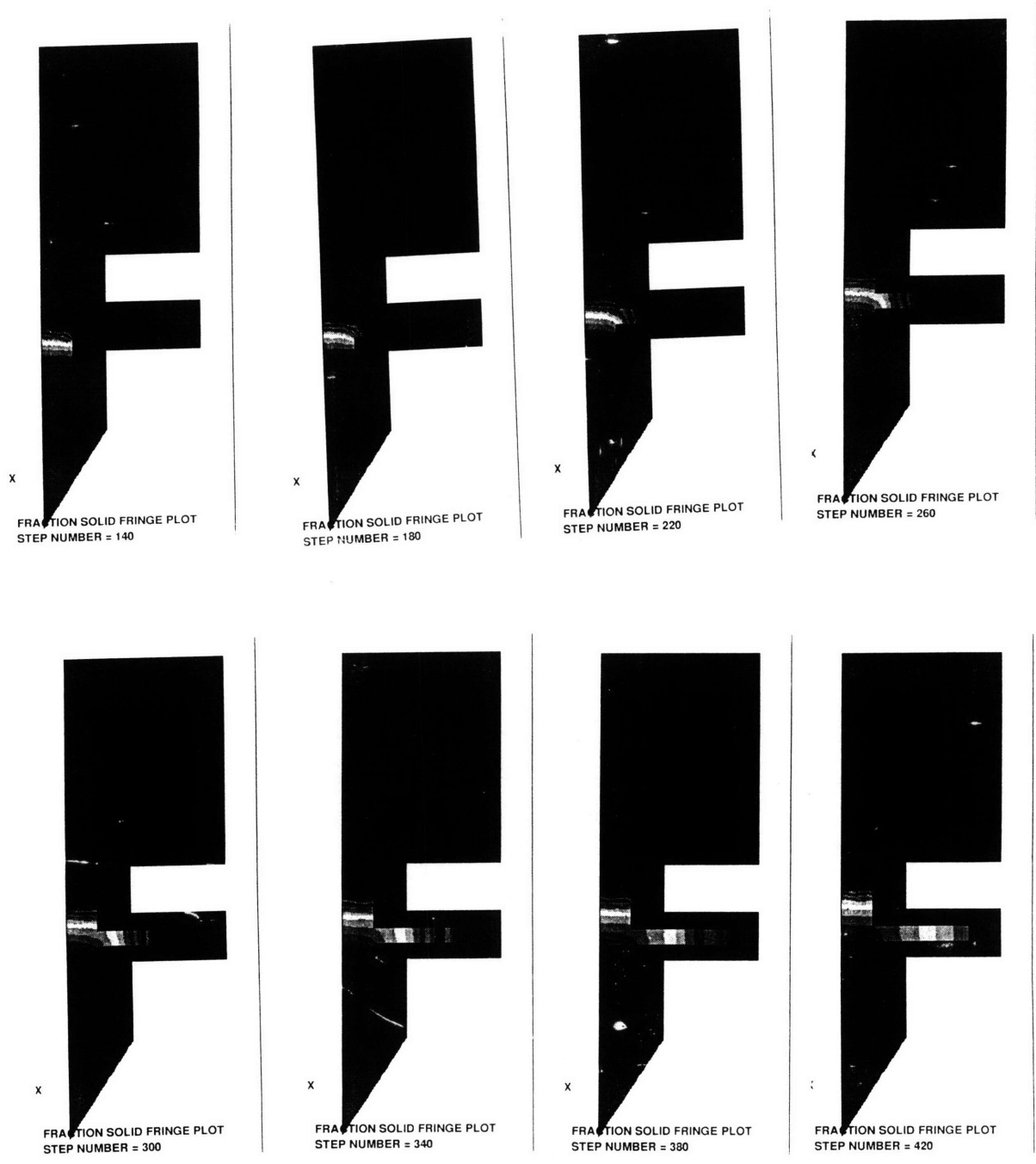
Fig.4-3. Solidification pattern of Al-4.5%Cu type 2. Fraction solid profiles.

80

FRACTION SOLID FRINGE PLOT
STEP NUMBER = 400

FRACTION SOLID FRINGE PLOT
TEP NUMBER = 600

FRACTION SOLID FRINGE PLOT
TEP NUMBER = 800

RACTION SOLID FRINGE PLOT
TEP NUMBER = 1000
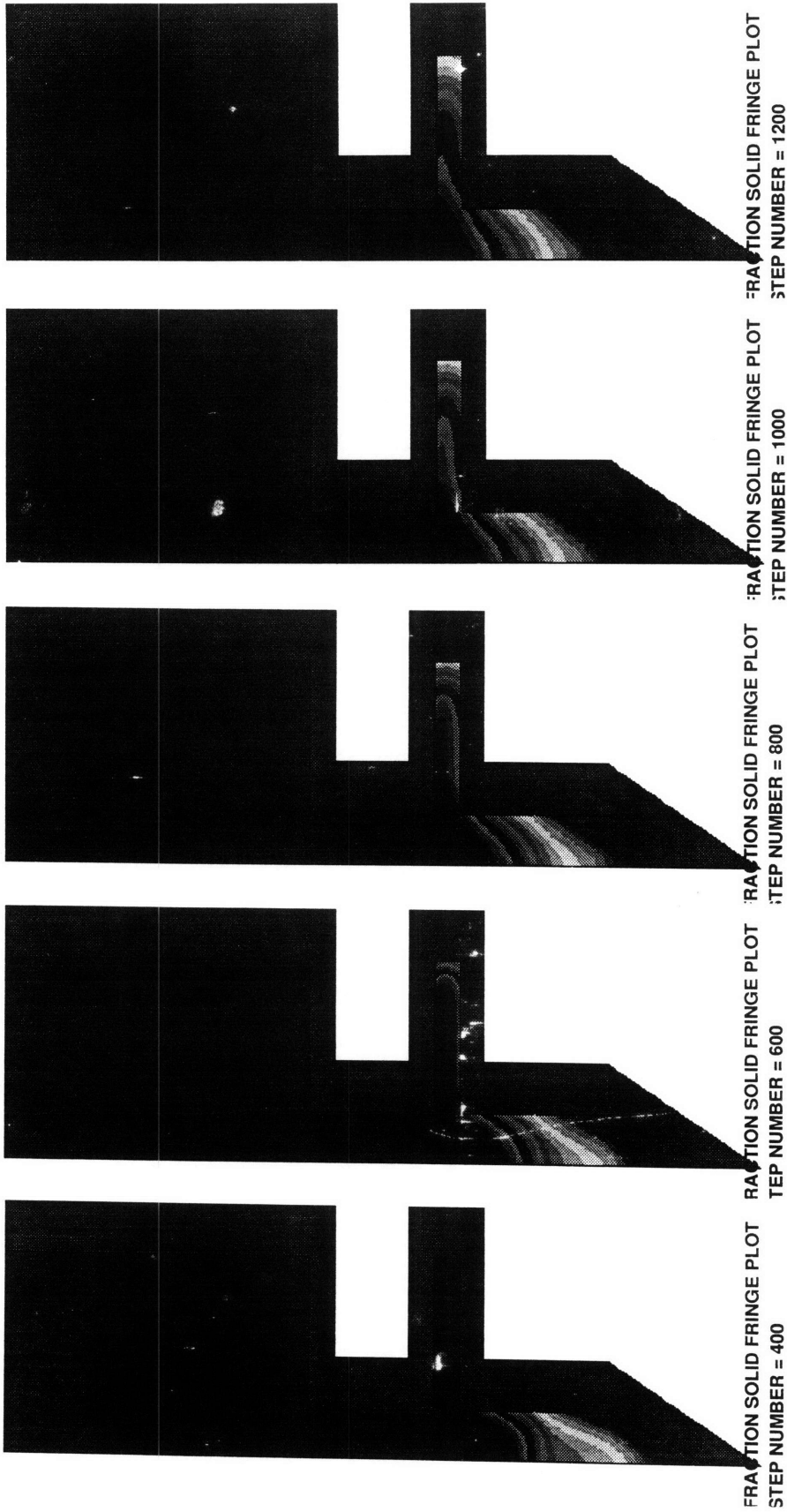
FRACTION SOLID FRINGE PLOT
STEP NUMBER = 1200

Fig. 4-4. Solidification pattern of Inconel 718 type 1. Solidificatoin starts from the outer edge of the platform before the main solidification front has reached the platform region.
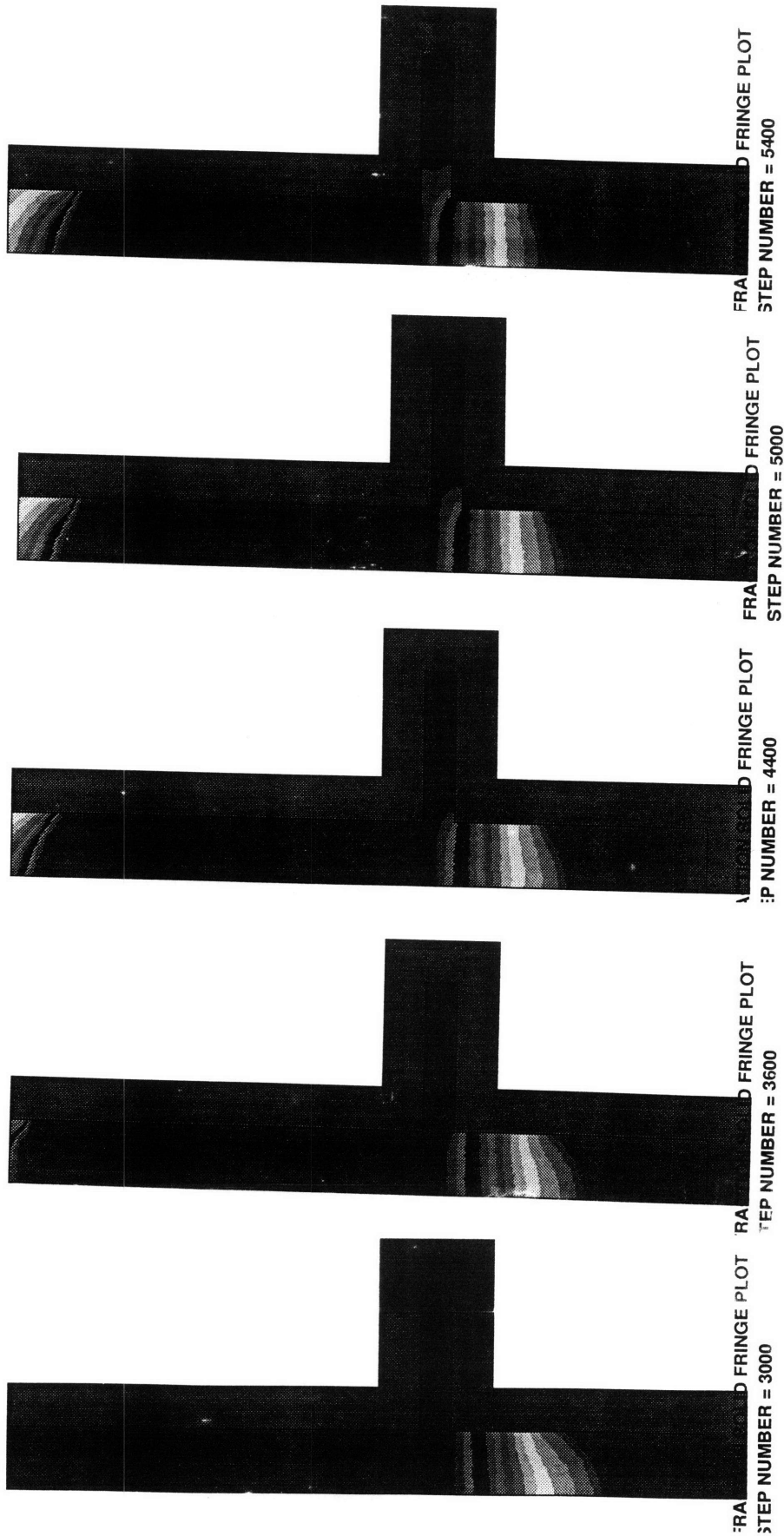
Fig.4-5. Solidification pattern of Inconel 718 type 2. The solidificatoin front is one line that fills the platform from the center of the casting towards the outer edge.

It would be very difficult to avoid defects caused by secondary and stray grains in the finished product for the solidification pattern shown in Figures 4-2 and 4-4, since the movement of the second solidification front is faster than that of the main one due to faster heat transfer in the platform region with increased cross-section. This faster heat transfer causes the second solidification front to spread throughout most of the platform region. That is, most of the solidified platform region will be made up of a stray grain. And the greater the lateral extension of the platform region from the main part of the casting, the earlier in the solidification process the second front will form. However, the relative speeds of the two fronts may be controlled to some extent by careful choice of processing conditions.

The second pattern of solidification front advancement (Figs. 4-3 and 4-5) has better probability of minimizing defects such as secondary grains for the finished product. In order to eliminate the potential for edge porosity under these conditions, a riser could be attached to it to contain the pores, to be cut out after the solidification. Or a thin tube, connecting the top section of the main part of casting to the end of the platform region, could be inserted in order to feed more material into the region as needed, thus minimizing pore formation.

The large number of numerical experiments in simulation of directional solidification for Al-Cu and In718 yielded other general trends. Among them were: the generated pictures of solid fraction, isotherms, and heat flux for the Inconel 718 had much more crisp lines than their counterparts for Al-Cu; the size of the mushy zone was much narrower for In718; and the total time for In718 solidification was considerably longer than that for Al-Cu. The narrower mushy zone of In718 agrees well with observations in an actual production process [41]. On the other hand, although longer solidification time is in good agreement with the time scale obtained in Section 3.6, it does not correspond well to

actual process, in which In718 has a much smaller solidification time. This longer solidification time given by the radiation-based method of calculation and simulation suggests that convective and conductive heat transfer may be more significant than expected for this temperature range, which may indicate the presence of turbulence in the system.

Another factor, though not as significant, may be the air flowing between the outer mold wall and the inner furnace wall. If the air velocity is high due to a large temperature gradient-induced convection, it will cool the mold temperature faster and speed up the solidification. The model assumed a vacuum between the mold and the furnace, leaving no room for any convection to occur in that region. With air between the mold and the furnace walls, simulated solidification time for In718 may decrease.

Finally, a simulation run with the time scale (actual) for completion on the order of a few hours, such as those described here, appears to be accurate enough to be able to display general changes in solidification patterns of a casting. For more greater accuracy of the resulting profiles, the time scale will increase, which may not be desirable when a quick prediction of solidification behavior is needed. Therefore, when choosing run parameters, consideration should be given both to the level of accuracy of the calculation and the efficiency of the simulation program.

4.4 Turbulence and Mold Filling

While the process analyses were performed assuming an initially filled mold, the filling process itself can often lead to defects in a casting. One such mechanism is transient melting and re-freezing at the solidification front due to turbulent temperature fluctuations, which results in a spot of low solute concentration. It is thus important to determine the

intensity of the turbulence during the filling process, and the relationship between its decay and the advance of the solidification front.

Figure 4-6 shows the cross section of a hypothetical turbine blade of varying thickness, and the associated turbulence decay time as a function of position, calculated for typical thickness of turbine blades (0.5 cm) and turbulent kinematic viscosity ($\sim$10$v_{,laminar}$) for Ni-based superalloys. The strong thickness dependence of decay time leads to a very strong peak in decay time in the thickest part of the casting, which will thus have the highest probability of defects. Figure 4-7 [42] shows the part of an isosceles wedge which is turbulent (above the curve) as a function of Reynolds, so that, for example, at a Reynolds number of 2000, flow will be turbulent from x/L=0.27 to x/L=1.

Figure 4-8 shows the geometry of a sample turbine blade created by the Patran code. Figures 4-9 and 4-10 show a simulation of liquid superalloy advancing into the mold, the former at an effective viscosity ten times the actual viscosity (to approximate the effect of turbulence), the latter at 100 times the actual value. Note that the predicted overall fill time does not differ considerably between the two. However, the Reynolds number at two points in the blade section differs considerably, as shown in figure 4-11. Simulated flow at the top of the blade reaches a peak Reynolds number of about 13000 at 10μ, and just 9000 at 100μ. At the bottom foil, the situation is reversed, but only because the flow in the former case reaches this point from the top and bottom at close to the same time.

The rapid decay of the Reynolds number in figure 4-11, and the relatively short calculated time scale for the decay of turbulence in figure 4-6, show that turbulence is gone by the start of solidification, and will probably not play a role in the generation of defects for parts as thin as turbine blades.
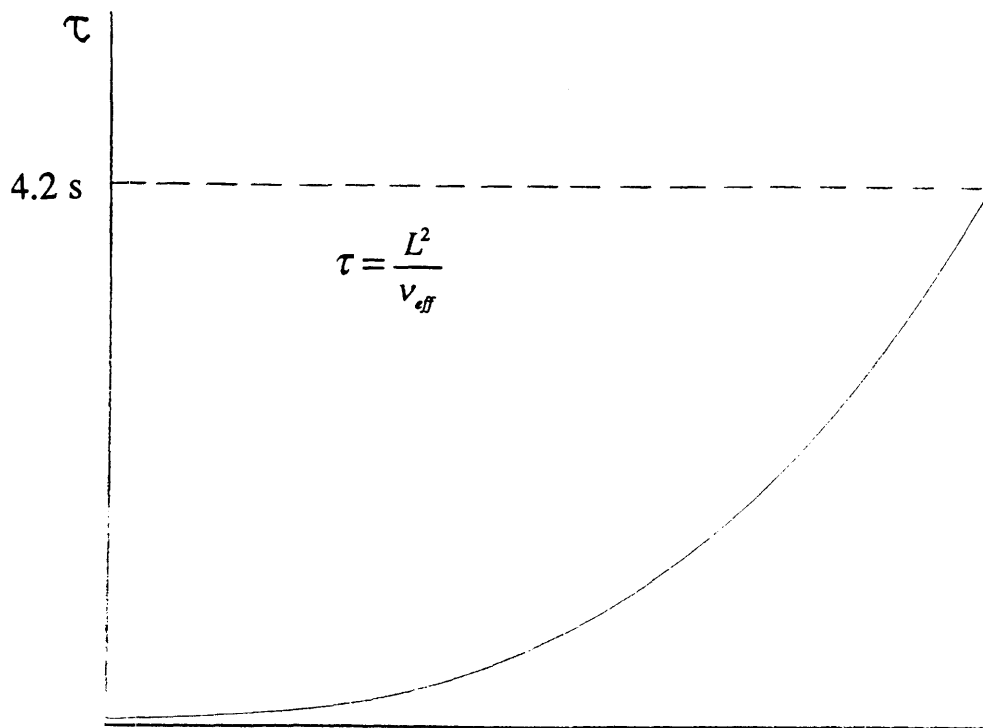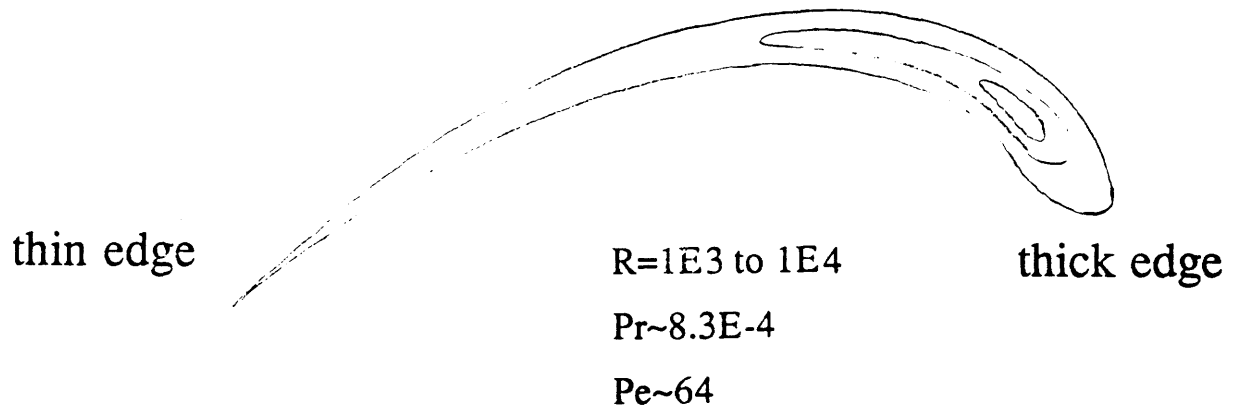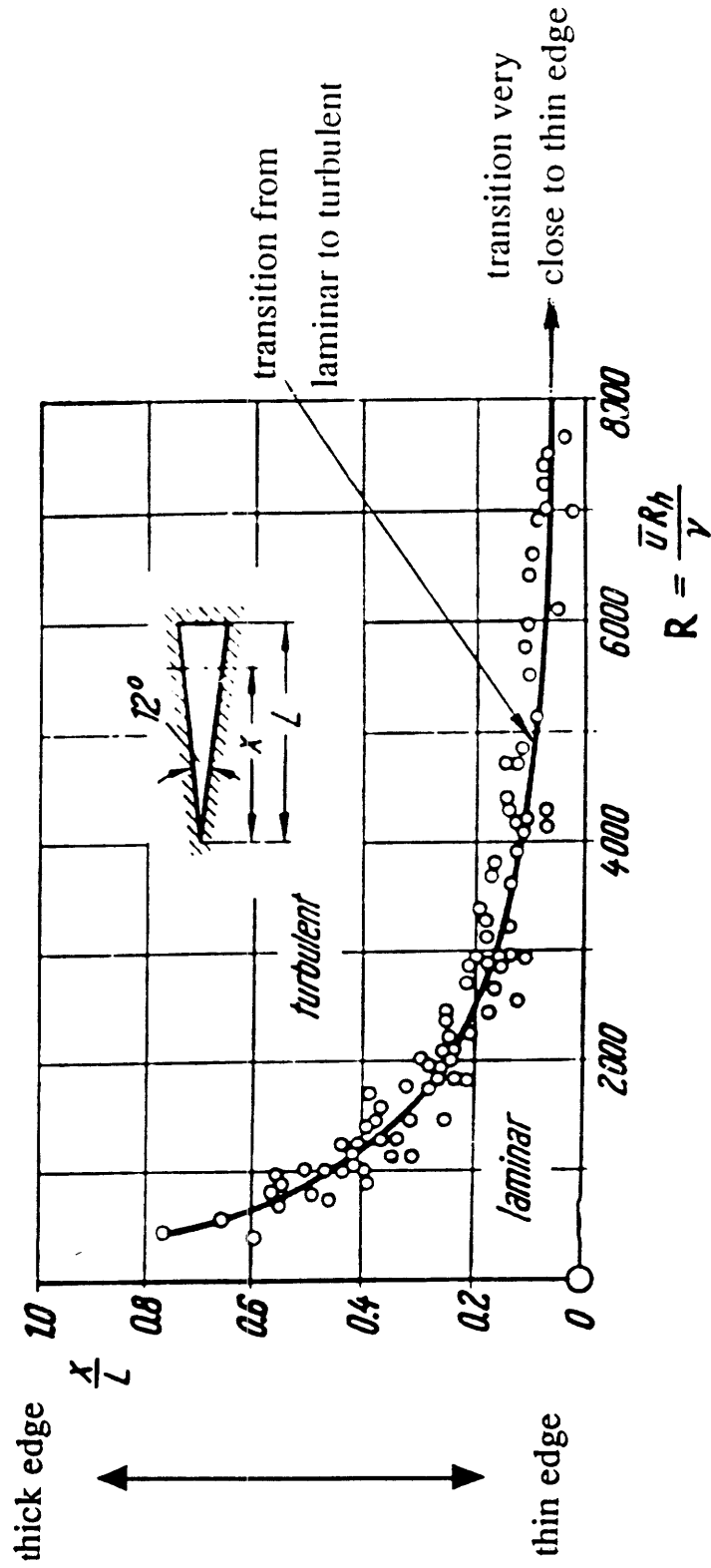
thin edge

R=1E3 to 1E4

Pr~8.3E-4

Pe~64

thick edge

τ

4.2 s

$$\tau = \frac{L^2}{\nu_{\it eff}}$$

Fig.4-6. Thickness-dependence of turbulence decay time.

Fig.4-7. Turbulent regime in turbine blades (laminar only on the thin edge).

R=1E3 to 1E4

(for equivalent circular pipe transition is at R=2300)

Fig.4-8. Geometry of turbine blade.

step number: 107
time: 0.514 s

step number: 100
time: 0.478 s

step number: 80
time: 0.401 s

FREESF: 1
EDGE: 0

$\mu = 10 \, \mu$

step number 70
time: 0.356 s

step number: 50
time: 0.256 s

step number: 30
time: 0.151 s
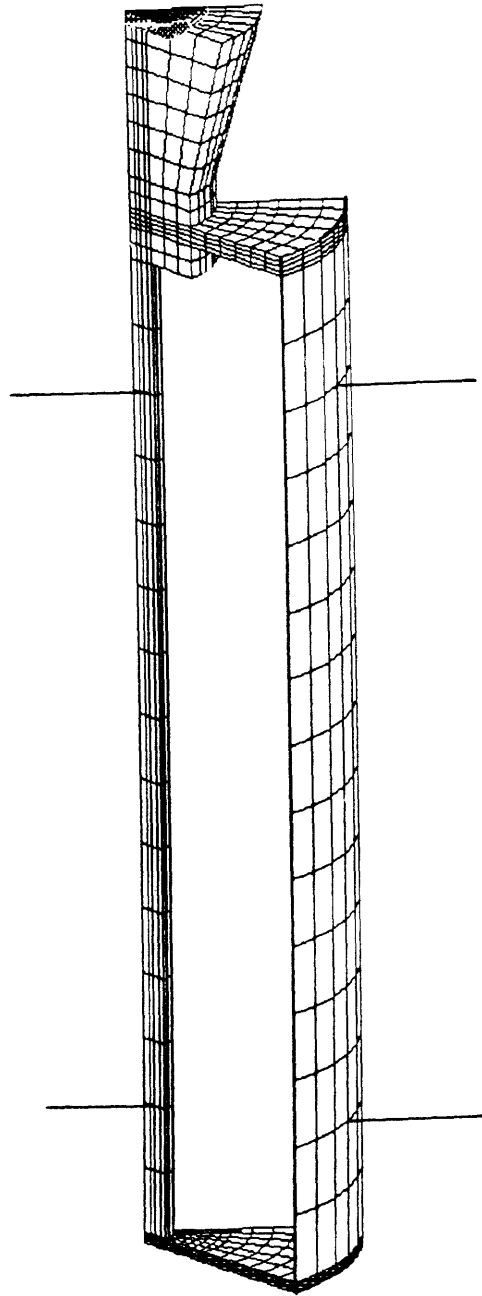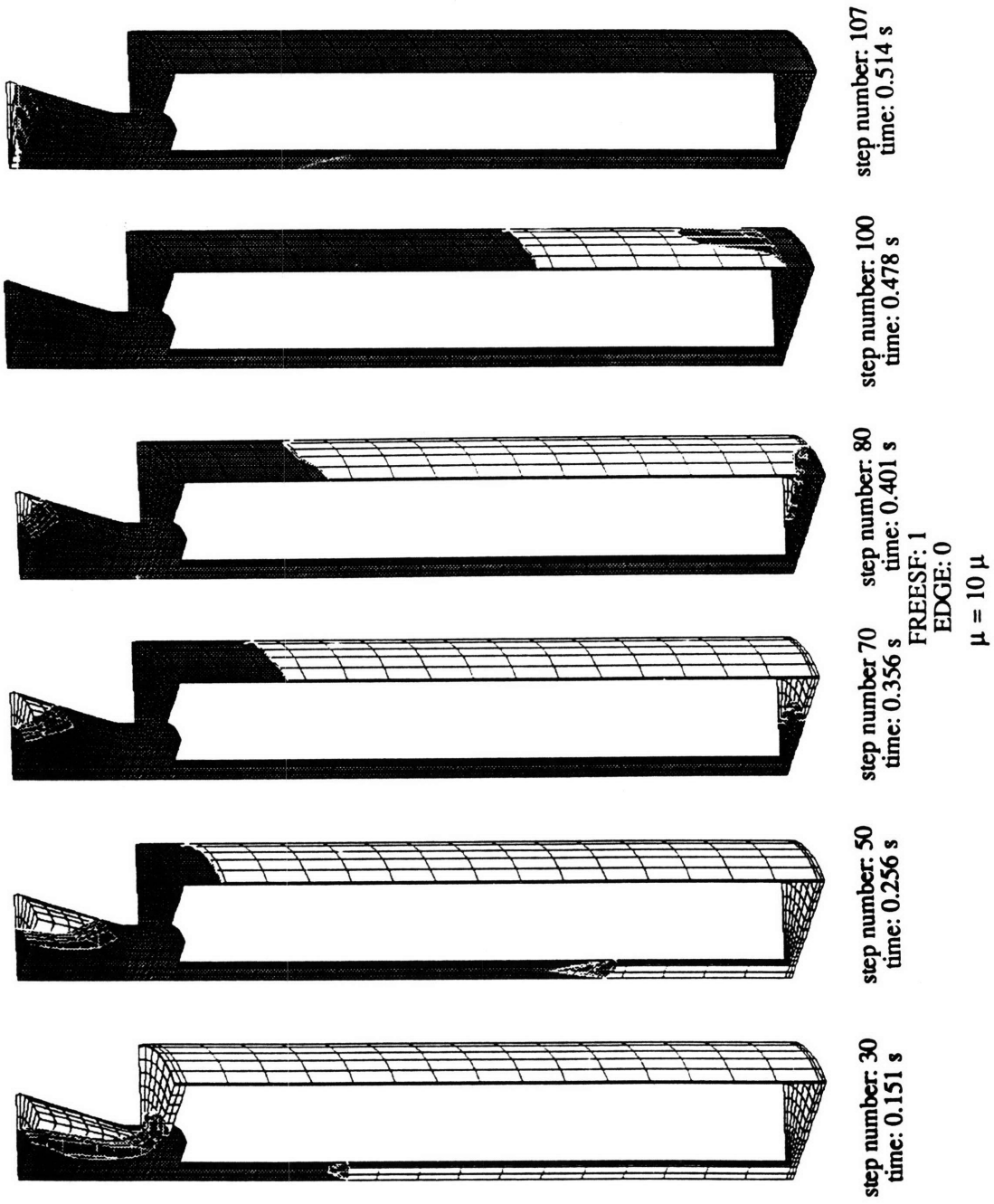
Fig.4-9. Mold filling pattern #1 of liquid superalloy.

step number: 30
time: 0.149 s

step number: 50
time: 0.254 s

step number 70
time: 0.356 s

step number: 90
time: 0.427 s

step number: 110
time: 0.497 s

step number: 113
time: 0.514 s
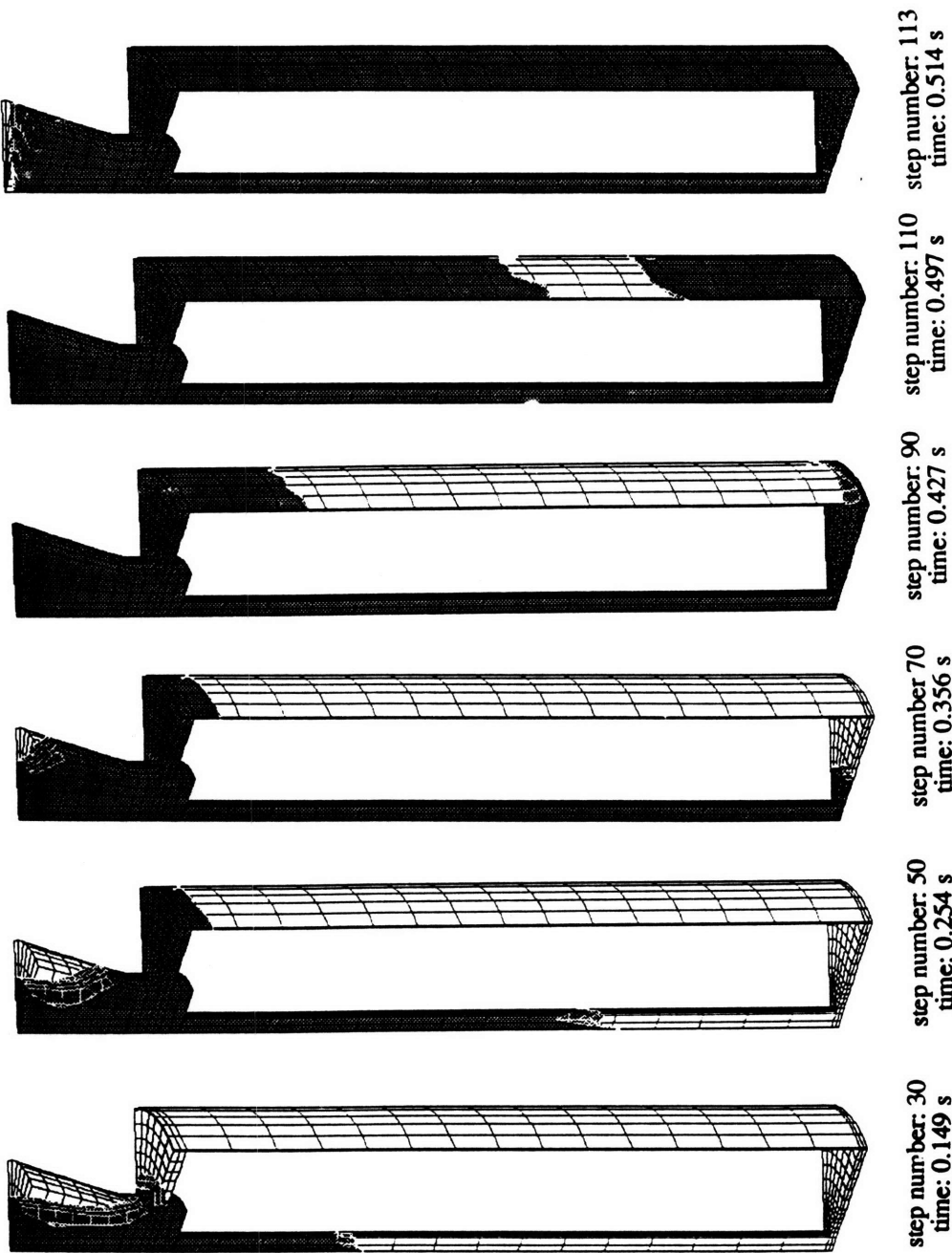
FREESF: 1
EDGE: 0

$\mu = 100\ \mu$

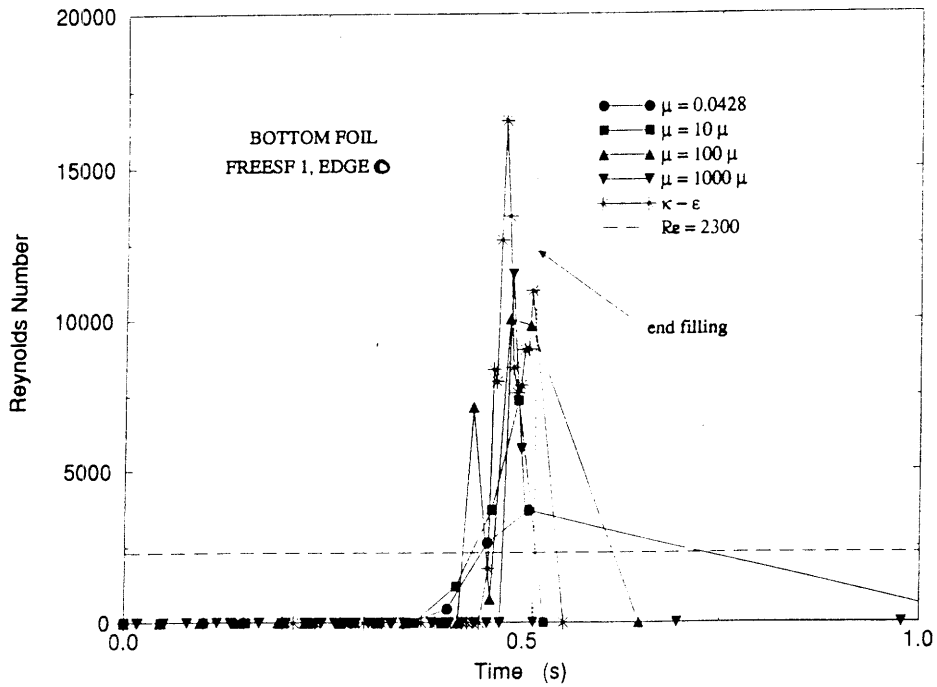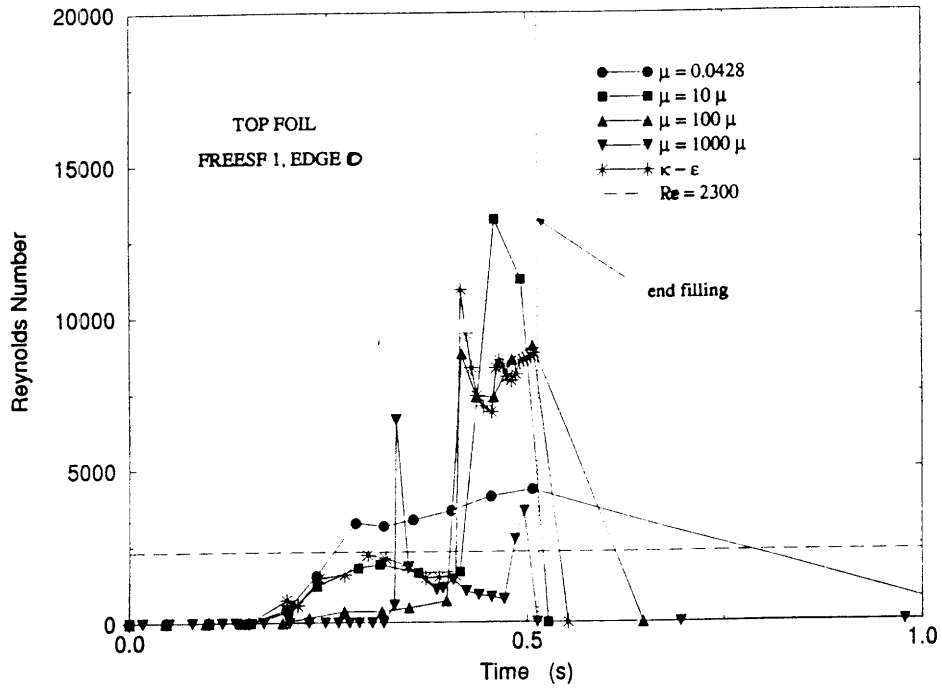Fig.4-10. Mold filling pattern #2 of liquid superalloy.

Fig.4-11. Reynolds number values for mold filling patterns shown
in Figs. 4-9 and 4-10.

4.5 Summary

ProCAST simulations were shown to agree well with experimental observations in terms of mushy zone thickness. However, further model refinement may be necessary to explain the discrepancy between calculations and experiments regarding overall solidification times. An important result from this study is that simulations proved to be very useful in the design of new process configurations which minimize the probability of nucleation and growth of secondary grains on the wider platform region of the casting. This methodology has the potential to be very important in the future design of directionally solidified casting equipment.

5. CONCLUSIONS

Mathematical and physical modelling were employed to study directional solidification of aerospace alloys during investment casting operations. The primary focus of this work was centered on the macroscopic aspects of transport phenomena in the platform region typically found in the complex geometry of turbine blade components. The main motivation for focusing on this specific region was to investigate the inherent formation of defects found the platform area, common in industrial production of such components but not well understood.

In the preliminary experiments using physical modelling of an aluminum-copper system, it was possible to study the effects of the main process characteristics. It was found that, by employing such an alloy system and stepwise geometric configurations, it was possible to reproduce similar behavior, in terms of formation of defects, as in the case of an actual prototype (a typical Ni-based superalloy produced by investment casting).

Estimations were made for the order of magnitude of different process parameters involved in directional solidification, in order to define possible flow regimes for both materials studied (i.e., Al-Cu system and Inconel 718). For the systems investigated, it was possible to establish the conditions necessary to minimize defect formation by avoiding convective turbulent regimes.

Computer simulation of the solidification process was performed for both materials to investigate the effects of different process conditions, such as imposed temperature

gradients and cooling arrangement (h), on the evolution of the solidification front. The analysis of a large number of "numerical experiments" (simulation runs) indicates that it is possible to control the solidification pattern around the cross-sectional change in the mold shape by careful designs of the solidification process with suitable values for relevant processing parameters.

6. RECOMMENDATIONS FOR FURTHER RESEARCH

The following is suggested for further studies of directional solidification of aerospace alloys using physical and mathematical modelling.

Physical Modelling

First, the results from the computational simulation of In718 solidification should be verified by physical modelling of In718 or another material with a similar melting range. It will also be useful to use geometric configurations whose scale is comparable to that used in actual manufacture lines, since the nature of a flow in a system depends greatly on the absolute magnitude of the characteristic length. Samples thus produced then should be given more extensive examination, so as to determine the specific differences, such as orientation and composition, between defect grains and the primary grains. Also, investigation of defect patterns on the platform regions of actual components should be continued, with the information obtained from the physical and mathematical modelling in mind.

Order of Magnitude Estimates

Mainly, the range of overall solidification time should be estimated, using different combinations of heat transfer mechanisms, to be compared to the time scale of casting in actual manufacture process. Information obtained from this step can be used in computational modelling as well.

Mathematical Modelling

More information can be obtained from computer simulation of directional solidification by incorporating micro-modelling in the simulation code. Attention should be paid, however, to program a run that can be completed in a relatively short period of time, for efficiency reasons. Given the rate of improvement in computational capabilities of computers, more complex programs may be run quickly, in the near future. Also, as suggested in Section 4.5, the total solidification time for In718 should be further investigated.

Finally, a specific ranges of optimum process conditions for casting materials should be obtained from the analyses that will help reduce formation of defects on the platform regions of turbine blades and other aerospace components with stepwise cross-sectional changes. Ultimately, a general procedure of effective and efficient modelling using both physical and numerical methods should be established to be used in various fields.

References

[1] E.W. Ross, GE EMTL, "Mantech for Advanced Propulsion Materials," Phase IX: Advanced Turbine A/F Casting Technology, 3rd Interim Report (1987).

[2] R. J. Schaefer, M. D. Vaudin, B. A. Mueller, C. S. Choi, and J. Szekely, "Generation of Defects in Single Crystal Components by Dendrite Remelting," in International Conference on the Modelling of Casting, Welding, and Advanced Solidification Processes VII (1995).

[3] Elihu F. Bradley, ed., Superalloys: A Technical Guide, ASM, Metals Park, OH (1988). p.17.

[4] Bradley, p.12.

[5] Th. Imwinkerlried, J.-L. Desbiolles, Ch.-A. Gandin, M. Rappaz, S. Rossman, and Ph. Thevoc, "Modelling of Dendritic Single Crystal Solidification at the Macro- and Microscopic Levels: Application to Turbine Blades," in Modelling of Casting, Welding, and Advanced Solidification Processes VI, eds. T.S. Piwonka, V. Voller and L. Katgerman, TMS (1993).

[6] Schaefer et al. (1995)

[7], [8], [9], [10], and [11] J. Szekely, Fluid Flow Phenomena in Metals Processing, Academic Press, New York (1979).

[12] W. Kurz and D. J. Fisher, Fundamentals of Solidification, Trans Tech Publications (1989). p.241.

[13] T. Iila and R. I . L . Guthrie, The Physical Properties of Liquid Metals, Clarendon Press, Oxford (1988).

[14] A. Cezairliyan, L. C. Phillips, R. A. McDaniel, A.Giamei, J. M. Peltier, R. A. Overfelt, and C. Y. Ho, "Thermophysical property data - Experimental Determination and Compilation," Consortium on Casting of Aerospace Alloys, NIST (Boulder, CO.) (1994).

[15] Iila and Guthrie (1988).

[16] Rappaz et al., p.66.

[17], [18] and [19] Kurz and Fisher, pp.238-246.

[20] T. B. Massalski, ed., Binary Alloy Phase Diagrams, 2e Vol. 1, ASM International (1990). p.142.

[21], [22], [23], and [24] Kurz and Fisher, pp.238-246.

[25] , [26], [27], and [28] Rappaz et al., pp.66-67.

[29] Kurz and Fisher, p.86.

[30] and [31] J. Szekely and N. J. Themelis, Rate Phenomena in Process Metallurgy, Wiley-Interscience, New York (1971).

[32] E. R. G. Eckert, <u>Analysis of Heat and Mass Transfer</u>, Hemisphere Pub. Corp. (1987).

[33] Y. Kawai and Y. Shiraishi, <u>Handbook of Physico-chemical Properties at High Temperatures</u>, The Iron and Steel Institute of Japan (1988).

[34] Szekely and Themelis (1971).

[35] and [36] ProCAST™ User's Manual, Version 2.1, UES, Inc.

[37] Cezairliyan et al.(1994).

[38] and [39] Y. S. Touloukian, ed., Thermophysical Properties of High Temperature Solid Materials, Vol. 4. The MacMillan Co., New York (1967).

[40] Cezairliyan et al.(1994).

[41] B. A. Mueller, R. Helmink, B. Bhat, D. Stewart, L. Graham, and M. Samonds, "Validation and Calibration," Consortium on Casting of Aerospace Alloys, NIST, 1994.

[42] Eckert, Trans. ASME, Irvine (1956). pp.709-718.

Appendix

Parameters used for Figures 4-2 through 4-5

Fig.4-2

h	200 ~ 7000 W/m·K
Cooling rate	4.72 K/min
ε	0.6 ~ 0.95
G	-1000 K/m

Fig. 4-3

h	1000 ~ 10000 W/m·K
G	- 600 K/m
ε	0.1 ~ 0.75
Cooling rate	4.5 K/min

Figs. 4-4 and 4-5

h

T (°C)	h (W/m·K)
200	1000
500	1000
800	2000
1000	3000
1100	4500
1144	5500

1234   9000

1334   10000

1580   10000

ε (emissivity)

T (°C)	ε
820	0.6
1050	0.5
1240	0.45
1440	0.42
1600	0.413
1820	0.42

G	-1000 K/m
Cooling rate	8.58 K/min